



Glioma invasion and its interplay with nervous tissue and therapy: A multiscale model

Martina Conte^{a,*}, Luca Gerardo-Giorda^a, Maria Groppi^b

^a BCAM - Basque Center for Applied Mathematics, Alameda de Mazarredo, 14, Bilbao - E-48009, Spain

^b Dipartimento di Scienze Matematiche, Fisiche e Informatiche, Università di Parma, Parco Area delle Scienze, 53/A, Parma - 43124, Italy



ARTICLE INFO

Article history:

Received 4 June 2019

Revised 23 September 2019

Accepted 18 November 2019

Available online 19 November 2019

Keywords:

Multiscale glioma modelling

Diffusion tensor imaging

Fiber distribution function

Anisotropic diffusion

Tumor response to therapy

ABSTRACT

A multiscale mathematical model for glioma cell migration and proliferation is proposed, taking into account a possible therapeutic approach. Starting with the description of processes occurring at the subcellular level, the equation for the mesoscopic level is formulated and a macroscopic model is derived, via parabolic limit and Hilbert expansions in the moment equations. After the model set up and the study of the well-posedness of this macroscopic setting, we investigate the role of the fibers in the tumor dynamics. In particular, we focus on the fiber density function, with the aim of comparing some common choices present in the literature and understanding which differences arise in the description of the actual fiber density and orientation. Finally, some numerical simulations, based on real data, highlight the role of each modelled process in the evolution of the solution of the macroscopic equation.

© 2019 Elsevier Ltd. All rights reserved.

1. Introduction

Gliomas are the most frequent types of primary brain tumors, originating from mutations of glial cells of the central nervous system. They can be classified by cell type and are rarely curable, in particular *Glioblastoma multiforme* (GBM), the most aggressive subtype, characterized by poor prognosis and a median survival rate that can reach up to 15–16 months with a standard treatment protocol (Wrensch et al., 2002). A common treatment for glioma includes surgical resection of the tumor mass followed by a combination of chemotherapy and radiation therapy. A complete resection, unfortunately, is often impossible: the highly infiltrative nature of the tumor cells, in fact, leads to strongly anisotropic spread, with heterogeneous and often disconnected finger-like patterns, and to an 'invisible' tumor outer border, undetectable with current medical imaging techniques. Hence, a deeper understanding of tumor migration and invasion phenomena is of paramount importance.

The invasion of glioma cells in the human brain tissue is a highly complex phenomenon that involves several processes at

different spatial and temporal scales: from the microscopic intracellular dynamics, through the intercellular level where individual cell behaviours are presented, up to the macroscopic setting for the cell population density description. The exact causes of these events are still not completely well understood; this shortcoming is due to their complex biology at the cellular and molecular level and in the interactions with the surrounding environment. Cell interactions with Extra-Cellular Matrix (ECM) and adjacent cells, combined with biochemical processes, support active cell movement. The latter takes place along preexisting brain structures, with a remarkable preference for myelinated fibers, blood vessels and white matter tracts. In particular, the role of glioma cell surface receptors, such as some types of integrins (Gritsenko et al., 2012; Giovanna and Kaye, 2007), is of great importance in the haptotactic movement. The interaction of such receptors with ECM components supports cell adhesion, spread and migration through the extracellular environment, influencing also cell growth, division and proliferation (Demuth and Berens, 2004; Huttenlocher and Horwitz, 2011; Bitsouni et al., 2018).

The highly anisotropic structures of the underlying nervous tissue (that influence tumor position, shape and extent in the brain) can be identified by medical imaging techniques, such as Magnetic Resonance Imaging (MRI) and Diffusion Tensor Imaging (DTI). MRI is, in general, very effective to obtain morphological information and microscopic reconstruction of the brain, providing good contrast between grey and white matter. Even though this technique is unable to completely identify their infiltration in the tissue, it is typically used to detect brain tumors and to follow up

Abbreviations: ECM, Extra-Cellular Matrix; GBM, Glioblastoma multiforme; MRI, Magnetic Resonance Imaging; DWI, Diffusion Weighted resonance Imaging; DTI, Diffusion-Tensor Imaging; FA, Fractional Anisotropy; VMF, Von Mises-Fisher; ODF, Orientation Distribution Function.

* Corresponding author.

E-mail addresses: mconte@bcamath.org (M. Conte), lgerardo@bcamath.org (L. Gerardo-Giorda), maria.groppi@unipr.it (M. Groppi).

their evolution. DTI is a special kind of Diffusion-Weighted magnetic resonance Imaging (DWI) that allows to map water molecule diffusion patterns, revealing microscopic details about tissue architecture. The detected differences in molecular mobility highlight the anisotropic effects, providing a description of the local physical arrangement of the medium and the eventual presence of obstacles or promoters of the movement. DTI is a highly valuable tool in glioma prognosis, since it provides information about the local tissue structure (Tuch et al., 2003), allowing to identify aligned structures along which cell migration is more likely to occur.

Mathematical modelling of tumor cell migration and invasion inside the tissue and, in particular, the modelling of GBM growth, evolution and treatment, has evolved significantly over the past years and several different approaches have been developed (Hatzikirou et al., 2005; Martirosyan et al., 2015; Alfonso et al., 2017; Byrne, 2010; Khajanchi, 2019). Models used for the description of glioma evolution can be classified into three main groups: discrete, hybrid and continuum models. *Discrete models* are used for the description of individual cells dynamics moving on a lattice (e.g., see Hatzikirou et al., 2012; Böttger et al., 2012 and references therein), while *hybrid models* involve both discrete and continuous equations, characterizing cell motion and the evolution of external factors, respectively (e.g., see Gevertz and Torquato, 2006; Tanaka et al., 2009; Kim and Roh, 2013; Frieboes et al., 2007; Khajanchi and Nieto, 2019). In the framework of *continuum models*, a significant number of studies rely on reaction-diffusion equations to characterize glioma density directly at a macroscopic scale. Starting from the work of Swanson et al. (2000), where the idea of spatially dependent isotropic diffusion coefficients has been introduced by two different constants for the description of the diffusion process in grey and white matter, a critical point has been the tuning of the model parameters to match model output to clinical data. A major improvement in this direction was given by linking the tensor describing tumor diffusion with the information provided by DTI (e.g., see Jbabdi et al., 2005; Konukoglu et al., 2010; Cobzas et al., 2009; Swan et al., 2018). Other *macroscopic models* for tumor migration rely on *mass conservation* (e.g., see Swanson et al., 2003; Swanson et al., 2008; Wang et al., 2009; Chaplain and Lolas, 2006; Anderson et al., 2000) and/or on *mechanical-chemical description*. The latter takes into account the forces exerted inside the tumor and at the interface between healthy and neoplastic tissue, and the relevant deformation effects (Konukoglu et al., 2010; Clatz et al., 2005; Bondiau et al., 2008; Barocas and Tranquillo, 1997; Maini, 1989). *Multiphase models* have been developed based on mixtures modelling, where the tumor description considers the malignant mass as a saturated medium, with at least one liquid phase (e.g., water) and one solid phase (e.g., glioma cells, ECM, etc.). Examples of this approach can be found in Tosin and Preziosi (2010), Ambrosi and Preziosi (2002), Colombo et al. (2015) and Agosti et al. (2018) and references therein.

A different approach consists in deducing the macroscopic model from a mesoscopic level of description of individual cell behaviour. These models use Boltzmann-type equations for the cell population density, where the usual collision operator describes the cell velocity changes. The resulting kinetic transport equation for the glioma cell density, in fact, does not depend only on time and space, but also on the (microscopic) velocity; a scaling argument is then used to derive the macroscopic setting (Hillen and Painter, 2013; Hillen, 2006; Painter and Hillen, 2013; Bellomo et al., 2012; Chauviere et al., 2007; Borcherding and McKinley, 2018). This approach has been extended to enhance the accuracy of the models, connecting the modelling of subcellular processes with the mesoscopic population-level description. This has been done within a *multiscale modelling* framework, in which the information emerging at the subcellular level introduces additional terms at the mesoscopic one and, consequently, in the macro-

scopic equations. In particular, this approach has been used to provide a more detailed description of the migration process, involving cellular receptors dynamics, as described in Lorenz and Surulescu (2014), Kelkel and Surulescu (2012), Meral et al. (2015) and Stinner et al. (2014), with a special focus on the case of glioma evolution (Engwer et al., 2016b; 2015; 2016a; Corbin et al., 2018).

In this paper we consider this last multiscale framework, modelling the growth and spread of glioma cells inside the brain tissue and highlighting the influence of the underlying nervous fibers on the tumor evolution. In particular, we focus on how the information about the fiber structures, obtained from the clinical data, is translated and encoded in the model to achieve a more realistic description of glioma cell spread and migration. Moreover, the role of the microscopic receptors dynamics in glioma evolution is investigated, as well as the tumor response to therapy.

The three different scales characterizing the processes and the model formulation follow a well-established modelling approach. At the *microscale*, as firstly proposed for the specific case of glioma in Engwer et al. (2015), we account for processes taking place at the subcellular level, governing the dynamics of bound receptors on the cellular membrane and described by an ODE for the mass action kinetics. At this scale, the novelty with respect to Engwer et al. (2015, 2016a) is the addition of therapeutic effects on the receptors dynamics. In particular, following the idea of Hunt and Surulescu (2017), a combination of chemotherapy and radiation treatment is considered (see also Chicoine and Silbergeld, 1995; Giese et al., 2003; Rockne et al., 2009 and references therein). At the *mesoscale*, we analyze the individual cell behaviours. They involve the interactions with the surrounding tissue, whose anisotropic characteristics are accurately taken into account, as well as the proliferation process and a loss term, that accounts for both the natural death of the cells and the radiation treatment. In particular, following the idea of Engwer et al. (2016a) and according to the general framework proposed in Bellomo et al. (2012, 2010), proliferation is included in the model, at this level, as a result of cell-tissue interactions. Finally, the *macroscopic* setting is derived via parabolic scaling of the mesoscopic equation, as done in Engwer et al. (2016b, 2015, 2016a) and Hunt and Surulescu (2017), yielding an evolution equation for the macroscopic cell density. In addition to the inclusion of therapeutic treatments modelling, the key point differentiating this work from previous ones (Engwer et al., 2015; 2016a; Hunt and Surulescu, 2017) is a novel and comprehensive comparison of the functions available in the literature for the description of the fiber structure, which plays an essential role in glioma dynamics. For the fiber description, we consider the Peanut distribution (Painter and Hillen, 2013) the Bimodal von Mises-Fisher Distribution (VMF) (Swan et al., 2018; Painter and Hillen, 2013; Mardia and Jupp, 2009) and the Orientation Distribution Function (Aganj et al., 2010). Such comparison, as well as the numerical simulations of the macroscopic model, have been done using real DTI data on a slice of brain reconstructed from MRI.

The paper is organized as follows. In Section 2, we describe the different processes and scales involved in the model, providing a formal derivation of the macroscopic setting and proving its well-posedness. Section 3 is dedicated to the analysis of the fiber distribution function that represents the connection between the diffusion tensor involved in the equations and the information provided by the MRI and DTI data (enabling their integration inside the model). In Section 4, different numerical simulations showing the dynamics of glioma cells in different scenarios are presented: first, the different fiber distribution functions described in Section 3 are tested to observe their effect on tumor evolution; then, we focus on the role of the subcellular dynamics; finally, we discuss the effect of the two specific treatments on tumor density. In Section 5, we comment on the main results of the model, its performance, and provide some concluding remarks. Details

about the anisotropy indices and the fiber distribution functions analyzed in this work are reported in the Appendices.

2. The model

Here we combine two different approaches, mainly presented in Engwer et al. (2016a) for the model set up and proliferation term description and in Hunt and Surulescu (2017) for the therapy description. In particular, the main differences with respect to Engwer et al. (2016a) are the introduction of the therapy description at the cellular level and the definition of a loss term in the mesoscopic equation for glioma cells. We define a formulation that starts from a description of cell receptor dynamics at the microscale and, adding a possible therapeutic approach, leads to an advection-diffusion-reaction equation at the macroscale.

2.1. Cellular level

At this level, we focus on the microscopic dynamics of cell surface receptors, like integrins, CD44 and ICAM-1 (Engwer et al., 2015). In particular, integrins are transmembrane receptors that facilitate cell adhesion, spread and migration binding to insoluble ligands of the underlying ECM. For simplicity, in the following we will refer to all cell surface receptors as integrins. Intending to understand the influence of integrin dynamics on the macroscopic movement at the tissue scale, we denote by $y(t)$ the concentration of bound integrins, depending on the time t ; we assume that the binding between integrins and tissue occurs preferentially in regions of highly aligned tissue (Engwer et al., 2015).

The description of the microscopic setting is taken from Engwer et al. (2015) and Hunt and Surulescu (2017) (to which we refer for a detailed explanation) and can be summarized as follows. The mass action kinetics for the concentration $y(t)$ is governed by the following ordinary differential equation:

$$\frac{dy}{dt} = k^+(d_c)(1-y)Q(x)S(\alpha_2, \beta_2, d_r) - k^-(d_c)y. \quad (1)$$

In this equation, $Q(x)$ indicates a time-invariant density field depending on the position $x \in \mathbb{R}^n$, and it represents the fraction of the insoluble component of the ECM involved in the integrin binding (Engwer et al., 2016b; 2015). The therapy effect is modelled through the terms $S(\alpha_2, \beta_2, d_r)$, $k^+(d_c)$ and $k^-(d_c)$. As in Hunt and Surulescu (2017) and Lefrank et al. (2005), $d_c(t)$ denotes the dose of chemotherapeutic treatment which affects cell invasion by influencing the interaction between integrins and ECM through the attachment and detachment rates $k^+(d_c)$ and $k^-(d_c)$. In particular, $d_c(t)$ reduces the capability of the cells to bind with the ECM. On the other hand, $d_r(t)$ represents the dose of radiotherapy, directly aimed at cell killing. We assume $d_c(t)$ and $d_r(t)$ to be at least piecewise continuous functions of time. In line with the well-established linear-quadratic radiobiological model (L-Q) (Sachs et al., 2001; Fowler, 1989; Brenner, 2008), the surviving fraction of cells after radiotherapy is given by

$$S(\alpha, \beta, d_r) = \exp(-\alpha d_r - \beta d_r^2) \quad (2)$$

where α and β represent the lethal lesions produced by a single radiation track or by two radiation tracks, respectively. We will use different values for the parameters α and β referring to tumor cells (α_1 and β_1) and to normal tissue (α_2 and β_2). In particular, we will indicate with $S_1(d_r) = S(\alpha_1, \beta_1, d_r)$ and $S_2(d_r) = S(\alpha_2, \beta_2, d_r)$.

Since the microscopic integrin dynamics is assumed to be much faster than the macroscopic time scale (hence to equilibrate rapidly Engwer et al., 2016a), we consider the unique steady state y^* of

Eq. (1):

$$y^* = \frac{k^+(d_c)Q(x)S_2(d_r)}{k^+(d_c)Q(x)S_2(d_r) + k^-(d_c)} \\ =: f(k^+(d_c), k^-(d_c), Q(x), S_2(d_r)). \quad (3)$$

Introducing a new internal variable $z(t) := y^* - y$, that measures the deviation of $y(t)$ from the steady state (Engwer et al., 2015), we look at the path of a single cell moving from an initial position x_0 with velocity v through the field $Q(x)$. With the notation $x = x_0 + vt$, Eq. (1) can be rewritten for the deviation $z(t)$ as (Hunt and Surulescu, 2017):

$$\frac{dz}{dt} = -z(t)(QS_2k^+ + k^-) + F(t) + \frac{\partial f}{\partial Q} v \cdot \nabla_x Q =: G(z, Q, d_c, d_r) \quad (4)$$

where $F(t) + \frac{\partial f}{\partial Q} v \cdot \nabla_x Q$ represents the total derivative of $f(k^+(d_c), k^-(d_c), Q(x), S_2(d_r))$ with respect to time.

2.2. Intercellular level

Using the above characterization of the microscopic dynamics, we describe the cell behaviour with the aid of velocity-jump processes. At this level, we stem from the model formulation proposed in Engwer et al. (2016a) (see the original work for a detailed introduction), and we add an overall loss term. Specifically, letting $\rho(t, x, v, z)$ be the glioma density function at time t , position $x \in \mathbb{R}^n$, velocity $v \in V \subset \mathbb{R}^n$, and internal state $z \in Z \subseteq [y^* - 1, y^*] \subset \mathbb{R}$, the kinetic transport equation for its dynamics is given by:

$$\begin{aligned} & \partial_t \rho + \nabla_x \cdot (v\rho) - \partial_z [G(z, Q, d_c, d_r)\rho] \\ &= \mathcal{L}[\lambda]\rho + P(\rho) - L(\bar{\rho}, R_1, d_r)\rho. \end{aligned} \quad (5)$$

Here, $\mathcal{L}[\lambda]\rho$ denotes the turning operator, a mathematical representation of the cell velocity changes. These changes are due in particular to contact guidance, which describes the oriented motility response of cells to the anisotropy of the environment. In the case of glioma cells, the movement and spread are especially associated with white matter tracts, acting as highways for their migration. $\mathcal{L}[\lambda]\rho$ is defined via an integral operator of Boltzmann type (Painter and Hillen, 2013)

$$\mathcal{L}[\lambda]\rho = -\lambda(z)\rho + \lambda(z) \int_V K(x, v)\rho(v')dv' \quad (6)$$

where $\lambda(z) := \lambda_0 - \lambda_1 z \geq 0$ is the turning rate, depending on the microscopic variable $z(t)$, while λ_0 and λ_1 are positive constants. In particular, since $y^* < 1$, $|z| < 1$ and we assume that $\lambda_0 \geq \lambda_1$ to ensure a positive turning rate. The term $\lambda(z)\rho$ represents the rate at which cells change their velocity v to any other velocity. The integral term denotes the cell changing from any velocity v' to velocity v . In order to model the turning kernel $K(x, v)$ in (6) we assume that the dominating directional cue is given by the oriented environment of the brain fibers and, consequently, cells choose their new direction according to the given fiber network. We describe the oriented structure of the environment by defining a directional distribution $q(x, \hat{v})$, with $\hat{v} \in \mathbb{S}^{n-1}$ (where \mathbb{S}^{n-1} denotes the unit sphere in \mathbb{R}^n) and with symmetry $q(x, \hat{v}) = q(x, -\hat{v})$. In this framework, assuming a constant cell speed (namely, $V = s\mathbb{S}^{n-1}$) the turning kernel is modelled as $K(x, v) = \frac{q(x, \hat{v})}{\omega}$, with scaling constant $\omega := \int_V q(\hat{v})d\hat{v} = s^{n-1}$ (Painter and Hillen, 2013; Engwer et al., 2015). In addition, if we associate integrin activation with cell binding to the tissue, we can see binding as the onset of proliferation and also of reorientation: in fact, the turning rate of the cells depends on the integrin state on the cell membrane. If many integrins are already bound, the cells will need to change their direction more often in order to escape from the too densely

packed fibers surrounding them (Sun et al., 2006), resulting in an increase in the rate $\lambda(z)$.

Following (Engwer et al., 2016a), we model proliferation as an effect of cell-tissue interactions via integrin binding; a way to include it at the mesoscopic level is to consider for the proliferation term $P(\rho)$ in (5) the form:

$$P(\rho) = \mu(x, \bar{\rho}, v) \int_Z \chi(x, z, z') \rho(t, x, v, z') Q(x) dz' \quad (7)$$

where $\bar{\rho} = \bar{\rho}(t, x)$ is defined by $\bar{\rho}(t, x) = \int_V \int_Z \rho(t, x, v, z) dz dv$ and $\mu(x, \bar{\rho}, v)$ denotes a general growth rate, for which specific forms can be chosen (see Section 4.2 for further details). In the integral operator, the kernel $\chi(x, z, z')$ characterizes the transition from state z' to state z during the proliferative process at position x . No particular conditions are required on χ . We only assume that the nonlinear proliferative operator $P(\rho)$ is uniformly bounded in the L^2 -norm, a reasonable biological condition linked to the space-imposed bounds on the cell division.

The overall loss is modelled by the last term in (5), as a combination of two parts: one term related to the natural death of the cells and one related to radiotherapy:

$$L(\bar{\rho}, R_1)\rho = (l(\bar{\rho}) + R_1(d_r))\rho. \quad (8)$$

In the clinical practice, the total dose of the drug is given in smaller fractions, to avoid toxic effects on healthy tissue. If ξ is the number of fractions, the total effect of the radiation therapy protocol can be expressed as:

$$R(\alpha, \beta, d_r) = \sum_{i=1}^{\xi} (1 - S(\alpha, \beta, d_r)) \eta_{\delta}(t - t_i) \quad (9)$$

where η_{δ} is a C_0^∞ function with unit mass and support in $(-\delta, \delta)$, $\delta \ll 1$, and t_i denotes the time instants at which an ionizing radiation is applied to the patient. In particular, following the notation introduced before, we will indicate with $R_1(d_r) = R(\alpha_1, \beta_1, d_r)$.

Global existence of a unique solution for Eq. (5) can be proved following the arguments in Lorenz and Surulescu (2014), under suitable growth conditions for the rate μ with respect to its third argument v .

2.3. Scaling of the mesoscopic equation

Considering the above analysis for the dynamics on the cellular and intercellular level, we start from Eq. (5) for the density $\rho(t, x, v, z)$. We introduce proper scaling arguments in order to deduce the macroscopic density equation, following the approach adopted in Engwer et al. (2015, 2016a) and Hunt and Surulescu (2017). Specifically, we consider the moments

$$\begin{aligned} m(t, x, v) &= \int_Z \rho(t, x, v, z) dz & M(t, x) &= \int_V m(t, x, v) dv (= \bar{\rho}(t, x)) \\ m^z(t, x, v) &= \int_Z z \rho(t, x, v, z) dz & M^z(t, x) &= \int_V m^z(t, x, v) dv. \end{aligned} \quad (10)$$

We do not consider higher order moments of ρ , as the subcellular dynamics is much faster than the events on the other scales so that the deviation z is close to zero. We also assume the data to be compactly supported in the phase space $\mathbb{R}^n \times V \times Z$. We first integrate equation (5) with respect to z and then multiply all terms in (5) by z and repeat the integration procedure. Then, we use a parabolic scaling $\hat{x} \rightarrow \epsilon x$ and $\hat{t} \rightarrow \epsilon^2 t$ for space and time variables, respectively. In particular, $F(t)$, which accounts for fast dynamics and involves time derivatives of d_c, d_r and of the cell survival fraction S , is scaled with ϵ^2 . Similarly, we scale the growth rate $\mu(x, M, v)$ and the loss term $L(M, R_1)$. Therefore, dropping the hat notation for simplicity, we obtain:

$$\epsilon^2 \partial_t m + \epsilon \nabla_x \cdot (v m) = -\lambda_0 m + \lambda_0 \frac{q}{\omega} M + \lambda_1 m^z - \lambda_1 \frac{q}{\omega} M^z$$

$$\begin{aligned} &+ \epsilon^2 \mu(x, M, v) \int_Z \int_Z \chi(x, z, z') \rho(t, x, v, z') Q(x) dz' dz \\ &- \epsilon^2 L(M, R_1) m \end{aligned} \quad (11)$$

and

$$\begin{aligned} \epsilon^2 \partial_t m^z + \epsilon \nabla_x \cdot (v m^z) &= -m^z (Q Sk^+ + k^-) + \epsilon^2 F(t) m \\ &+ \epsilon f'(Q) v \cdot \nabla_x Q m + -\lambda_0 m^z + \lambda_0 \frac{q}{\omega} M^z + \epsilon^2 \mu(x, M, v) \\ &\times \int_Z \int_Z z \chi(x, z, z') \rho(t, x, v, z') Q(x) dz' dz + \\ &- \epsilon^2 L(M, R_1) m^z. \end{aligned} \quad (12)$$

By applying the asymptotic Hilbert expansions of the moments of ρ (Chauviere et al., 2007; Othmer et al., 2000) and by collecting the coefficients of the different powers of ϵ in Eqs. (11) and (12), we obtain, at leading order, $M_0^z = 0$, $m_0^z = 0$ and $m_0 = \frac{q}{\omega} M_0$. As a consequence, $M_1^z = 0$ and, using compactness properties, it is possible to deduce that $M_1 = 0$ and

$$m_1 = \frac{1}{\lambda_0} \left[\frac{\lambda_1}{\lambda_0 + k^+ Q S + k^-} \frac{\partial f}{\partial Q} \nabla_x Q \cdot v \frac{q}{\omega} M_0 - \nabla_x \left(v \frac{q}{\omega} M_0 \right) \right]. \quad (13)$$

Finally, with these positions, we obtain by standard arguments (Engwer et al., 2015; 2016a) the following simplified form of the evolution equation for the macroscopic glioma density M_0 :

$$\begin{aligned} \partial_t M_0 - \nabla \cdot (D_T(x) \nabla M_0) + \nabla \cdot ((g(Q(x)) D_T(x) \nabla Q - u(x)) M_0) \\ = \mu(x, M_0) Q(x) M_0 - L(M_0, R_1) M_0. \end{aligned} \quad (14)$$

Here, we assume that the growth rate μ does not explicitly depend on v , and we denote by

$$g(Q(x)) := \frac{\lambda_1}{\lambda_0 + k^+(d_c) Q S_2(d_r) + k^-(d_c)} \frac{\partial f}{\partial Q}$$

the function carrying the information about the influence of the subcellular dynamics. The macroscopic diffusion tensor is expressed as

$$D_T(x) := \frac{1}{\omega \lambda_0} \int_V v \otimes v q(x, \hat{v}) dv \quad (15)$$

and the tumor drift velocity is given by

$$u(x) := \frac{1}{\omega \lambda_0} \int_V v \otimes v \nabla_x q(x, \hat{v}) dv. \quad (16)$$

It is important to stress that, even though the similarity between the macroscopic setting proposed in Engwer et al. (2016a) and Eq. (14) are evident, there are substantial differences in the modelling of the therapeutic approach, which follows the approach in Hunt and Surulescu (2017). More precisely, therapy has been introduced at the microscale (see Section 2.1) and its effects on the macroscopic equation (14) are collected in the terms $L(M_0, R_1)$ and $g(Q(x))$.

2.4. Well-posedness of the macroscopic setting

Using the theory of monotone operators for non-linear parabolic equations and following a well-known approach (Ruzicka, 2006; Showalter, 2013), it is possible to prove the existence, uniqueness and non-negativity of the solution of the parabolic problem (14) with homogeneous Neumann boundary conditions.

Let $\Omega \subset \mathbb{R}^3$ be a Lipschitz domain and \hat{n} the normal vector to $\partial\Omega$. Let $T > 0$ be finite and consider the following non-linear

parabolic initial-boundary-value problem related to Eq. (14):

$$\begin{cases} \partial_t M - \nabla \cdot (D_T(x) \nabla M) + \nabla \cdot (Y(Q, D_T) M) + \Gamma(M) = 0 & \text{in } [0, T] \times \Omega \\ \nabla M \cdot \hat{n} = 0 & \text{on } [0, T] \times \partial \Omega \\ M(0, x) = M_0(x) & \text{in } \Omega \end{cases} \quad (17)$$

where

$$\begin{aligned} Y(Q, D_T) &= g(Q(x)) D_T(x) \nabla Q - u(x) \\ \Gamma(M) &= ((l(M) + R_1(d_r)) - \mu(x, M) Q(x)) M. \end{aligned} \quad (18)$$

Adapting the proof proposed in Appendix A.1 of Engwer et al. (2016a), it is possible to prove the following theorem.

Theorem 1. Assume:

- A.1 The tensor $D_T(x)$ is uniformly positive definite, it belongs to the space $W^{1,\infty}(\Omega)$ and its smallest eigenvalue is larger than a constant $\alpha > 0$;
- A.2 $\Gamma(M)$ is continuous in time and M , it satisfies the growth condition $|\Gamma(s)| \leq c(1 + |s|^{r-1})$ for some $r \geq 1$ (with a constant c independent of time and space) and the coercivity condition $\inf_{s \in \mathbb{R}^+} \Gamma(s)s > -\infty$;
- A.3 The function $Q(x)$ belongs to the space $W^{1,\infty}(\Omega)$;
- A.4 The rates k^+ and k^- are continuous in the variable d_c (which in turn has to be continuous in time) and uniformly bounded;
- A.5 The term $Y(Q, D_T)$ is in $L^\infty(\Omega)$.

Let $U = H^1(\Omega)$, $H = L^2(\Omega)$ and $X = L^2(0, T; U)$ and let define the functional space

$$W := \{\omega \in L^2(0, T; U) : \omega_t \in L^2(0, T; U^*)\} \subseteq X.$$

Let $M_0 \in H$ and let $\Gamma : \mathbb{R} \rightarrow \mathbb{R}$ be a continuous function that satisfies the conditions A.2 above with $1 \leq r < \frac{10}{3}$. Then there exists a weak solution $M \in W$ of the problem (17), i.e., there exists $M \in W$ such that for all $\varphi \in C_0^\infty([0, T] \times \Omega)$:

$$\begin{aligned} &\int_0^T \langle \partial M_t, \varphi \rangle_{H^1(\Omega)} dt + \int_0^T \int_\Omega (D_T \nabla M - Y(Q, D_T) M) \nabla \varphi dx dt \\ &+ \int_0^T \int_\Omega \Gamma(M) \varphi dx dt = 0. \end{aligned}$$

It is also possible to prove uniqueness and non-negativeness of the solution, using classical estimates, parabolic comparison principle (Fangliang, 2012) and theorems from Section III.4.1. in Showalter (2013).

Proposition 1. The solution of the macroscopic problem (17) is unique if $\Gamma(M)$ is strictly monotone. In addition, if $M_0 \geq 0$, the solution of (17) is nonnegative.

3. Fiber distribution function

The analysis of the connection between the DTI data introduced in the model, the way in which they are processed and how their features are taken into account, is fundamental to obtain reliable simulations of tumor dynamics from both qualitative and quantitative point of view.

In this section, we investigate the way in which the fiber distribution function $q(x, \hat{v})$ incorporates in the model the information about the diffusivity in the brain and the anisotropic characteristics of the nervous tissue.

The fiber distribution density function $q(x, \hat{v})$ represents the link between raw data, collected in the symmetric 3D water diffusion tensor $D_W(x)$, and the tumor diffusion tensor $D_T(x)$, which describes tumor movement and diffusivity in the model equation. The function $q(x, \hat{v})$ is used to describe the probability of turning

at point x and into a normalized velocity \hat{v} , and it can be derived in different ways according to possible underlying distributions. Since the vector \hat{v} belongs to the unit sphere \mathbb{S}^{n-1} , for simplicity in the notation we will indicate it with the direction θ and, consequently, the fiber distribution function with $q(x, \theta)$. Three main choices of the fiber distribution $q(x, \theta)$ exist in the literature: the Peanut Distribution (Painter and Hillen, 2013), the Bimodal von Mises-Fisher Distribution (VMF) (Swan et al., 2018; Painter and Hillen, 2013; Mardia and Jupp, 2009) and the Orientation Distribution Function (ODF) (Aganj et al., 2010). They are defined as:

$$q(x, \theta) = \frac{3}{|\mathbb{S}^2| \operatorname{Tr} D_W(x)} \theta^T D_W(x) \theta \quad (\text{Peanut}) \quad (19)$$

$$q(x, \theta) = \frac{\delta}{4\pi} + (1 - \delta) \frac{k(x)}{4\pi \sinh k(x)} (\cosh(k(x)\phi_1 \cdot \theta)) \quad (\text{Bimodal VMF}) \quad (20)$$

$$q(x, \theta) = \frac{1}{4\pi |D_W(x)|^{\frac{1}{2}}} (\theta^T (D_W(x))^{-1} \theta)^{-\frac{3}{2}} \quad (\text{ODF}). \quad (21)$$

For the sake of completeness, we describe in details these distributions in Appendix B–Appendix D, respectively. In the rest of the section, we analyze and compare these distributions. We will highlight their specific capabilities to accurately reproduce the anisotropic characteristics of the underlying nervous tissue, their strengths and their weaknesses. We rely on the fractional anisotropy index FA (see Appendix A for its formal definition and properties), which gives a measure of the degree of anisotropy of the tissue, as an objective classifier to understand and compare how the information provided by the DTI data and encoded in the water diffusion tensor D_W are translated and preserved into the model.

3.1. Comparison of $q(x, \theta)$ on a single data point

For the sake of clarity in visualization, we first consider in two dimensions a single spatial point x and through equation (15) we

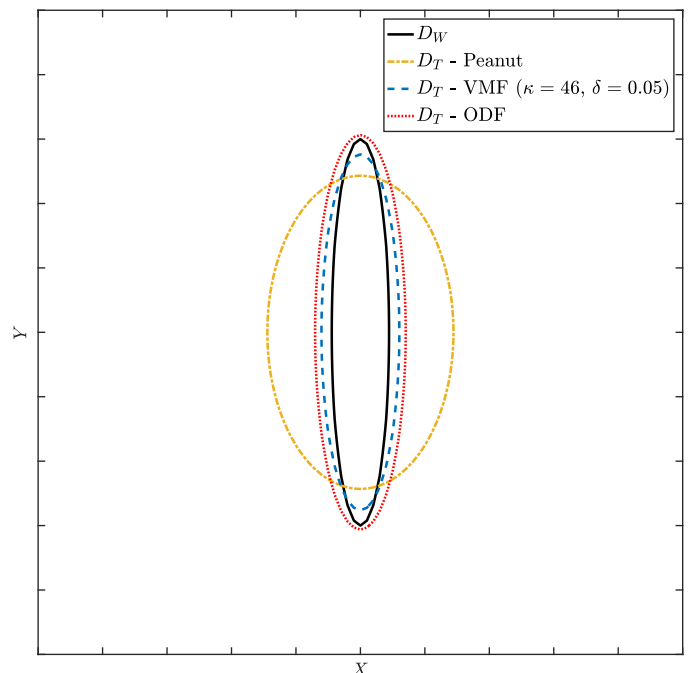


Fig. 1. $D_W(x)$ and $D_T(x)$ at the point x (For interpretation of the references to color in all the Figures, the reader is referred to the web version of this article.).

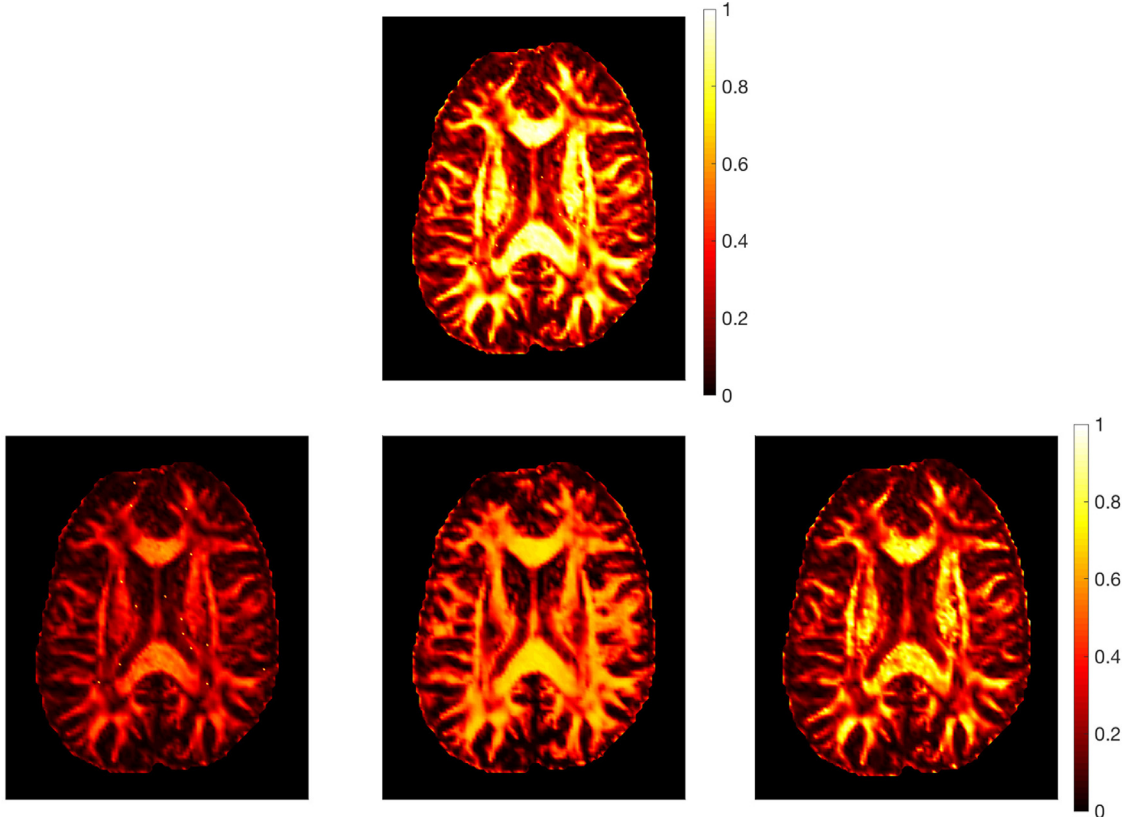


Fig. 2. Top row: $FA(D_W)$. Bottom row: from left to right, $FA(D_T)$ with Peanut distribution, VMF distribution with $\delta = 0.05$ and $\kappa = 5.7753$, and ODF.

compute D_T from D_W with the three different functions $q(x, \theta)$. We consider an anisotropic tensor D_W and assume for D_W a bigger diffusion along the y -axis direction than along the x -axis one. By visualizing the tensors as ellipses, it is possible to immediately grasp the difference between the way the three distributions reproduce the original anisotropy, as illustrated in Fig. 1.

With the Peanut distribution (19), the anisotropy of D_W is in large part lost in the resulting D_T tensor, due to the strong isotropic component of D_T (see B.2 for details). On the other hand, the tumor diffusion tensor D_T obtained with the VMF distribution (20) shows a degree of anisotropy much more similar to that of the original D_W . The similarity depends on the particular choice of the two parameters, κ and δ which require a preliminary optimization procedure (see Appendix C for details). Finally, with the ODF (21), the resulting D_T has once again similar shape and proportions to the original D_W . More pronounced preservation of the anisotropic characteristics with respect to the Peanut distribution case is clearly observed. Moreover, the independence from the parameter value selection gives an additional benefit with respect to the VMF distribution if no real patient data are available for an accurate estimation of these parameters.

For the Peanut distribution it has been proved analytically in Painter and Hillen (2013) that $FA(D_T) \leq FA(D_W)$, namely, the anisotropy in D_T is always lower than the anisotropy of the original tensor D_W . Therefore, with this particular distribution choice D_T may not be able to reproduce the brain structure accurately, especially in the case of crossing fiber tracts.

For the VMF distribution, on the other hand, in the limit for $\delta \rightarrow 0$ and $\kappa \rightarrow \infty$, one formally obtains that $FA(D_T) \rightarrow 1$, giving in principle the possibility to accurately reproduce the anisotropic characteristics of the tissue.

3.2. Comparison on real brain data

Here we compare the impact of the different fiber distribution functions (19)–(21) on real DTI data. The dataset was acquired at the Hospital Galdakao-Usansolo (Galdakao, Spain), and approved by its Ethics Committee: all the methods employed were in accordance to approved guidelines. We processed the DTI data using FSL (FMRIB Software Library)¹ Jenkinson et al. (2012), a comprehensive library of analysis tools for MRI and DTI brain imaging data.

For our comparison, we consider a 2D slice obtained from a horizontal section of an entire brain DTI dataset, as it is sufficiently representative for the proposed analysis. In order to give an objective comparison of the different fiber distribution functions, and to classify their goodness, we computed the fractional anisotropy $FA(D_W)$ and $FA(D_T)$, for the D_T obtained with the three distributions. The results are shown in Fig. 2.

What clearly emerges is that the use of the Peanut distribution identifies accurately the locations where the fibers are aligned or not, without significant over- or under-estimations of these areas. However, its main issue is related to the degree of anisotropy: in fact, the resulting tumor diffusion tensor D_T (B.2) shows a degree of anisotropy significantly lower than the original D_W , with values for the fractional anisotropy almost halved in the areas of greater alignment. For the VMF distribution the results are highly dependent on the parameters κ and δ , whose effect can be observed in greater details in Figs. C.13 and C.14 of Appendix C. Overall, the VMF distribution provides an over-estimation of the extension of the anisotropic regions, while depending on the calibration of κ and δ , there can be an over- or an under-estimation of the degree of anisotropy. Fig. 2 highlights good preservation of the

¹ Information available from <https://fsl.fmrib.ox.ac.uk/fsl/fslwiki/FSL>

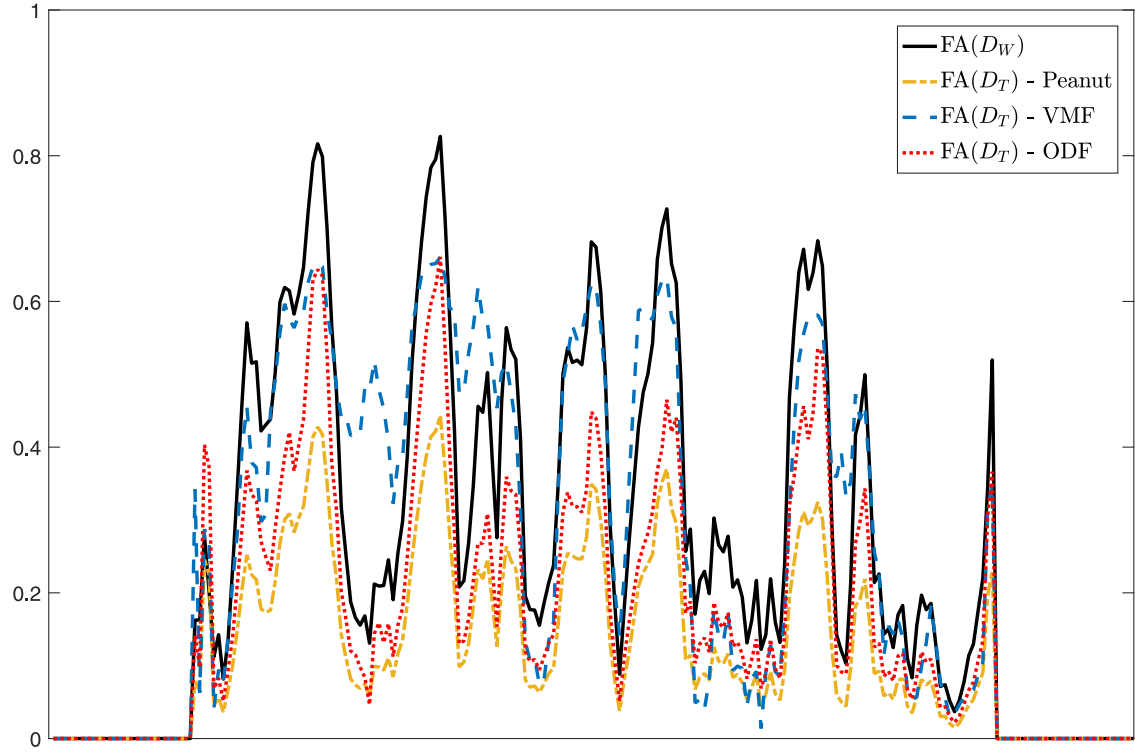


Fig. 3. Comparison between $FA(D_W)$ and $FA(D_T)$ along a coronal plane of the 2D brain slice. For the VMF distribution $\delta = 0.05$ and $\kappa = 5.7753$.

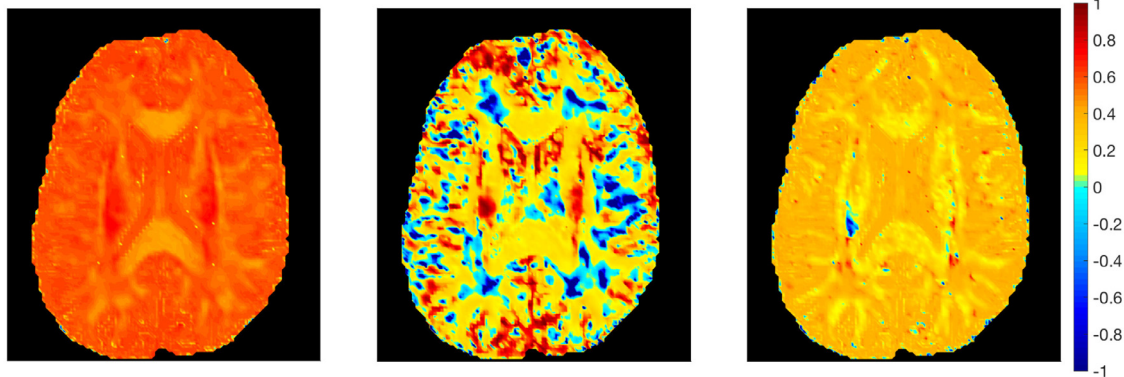


Fig. 4. From left to right, $R(D)$ for Peanut distribution, VMF distribution with $\delta = 0.05$ and $\kappa = 5.7753$ and ODF.

FA in the case of the VMF distribution, provided that a suitable tuning of its parameters is performed (if biological data are available, as explained in [Appendix C](#)). This tuning affects the description of the geometry features and, thus, we suppose it might have some influence on the evolution of the tumor dynamics. In particular, the values of the parameters κ and δ used for the analysis have been chosen through the optimization procedure described in [Appendix C](#). Finally, although the use of the ODF provides a general under-estimation of the degree of anisotropy, this distribution highly improves the results compared to the Peanut distribution, and it preserves with sufficient accuracy the description of the location of aligned and non-aligned fibers.

A closer look at the differences between the three distributions can be done by considering different coronal sections of this 2D slice and looking at the variation of the fractional anisotropy along them. In [Fig. 3](#) the comparison between $FA(D_W)$ and $FA(D_T)$ is shown for a representative coronal section.

As it can be noticed in [Fig. 3](#), Peanut distribution and ODF have an almost identical trend, but, as expected, the Peanut distribution

almost halves the degree of anisotropy with respect to the original data, while the ODF preserves it significantly better. VMF distribution, on the other hand, often provides an under-estimation of the fractional anisotropy at local maxima of $FA(D_W)$ and an over-estimation of $FA(D_W)$ on local minima. Changing the considered coronal section, the qualitative results do not change and the highlighted differences in the fractional anisotropy remain essentially the same.

In order to have a more global perspective, we consider the relative difference between the FA of the original data D_W and the one related to the tumor diffusion D_T , given by:

$$R(D) = \frac{FA(D_W) - FA(D_T)}{FA(D_W)}. \quad (22)$$

Notice that in (22) we are not considering the absolute value of the numerator in order to visualize situations of both under-estimation and over-estimation of the fractional anisotropy. The value of $R(D)$ for the considered distributions are shown in [Fig. 4](#).

In line with the results of Fig. 3, except for some isolated blue areas in the ODF plot (possibly related to errors in the measurements and/or to oscillations in the calculations), we observe that the VMF distribution is the only one with a markedly mixed trend. $R(D)$ for this distribution indicates that $FA(D_T)$ values pass from areas of over-estimation of the original anisotropy (colours from green to blue) to areas of under-estimation of the original FA (colours from green to red). An additional piece of information emerging from the comparison between the top row of Figs. 2 and 4 is that in the highly anisotropic areas, where $FA(D_W)$ is bigger, the relative error made with any of the three distributions is generally smaller with respect to more isotropic regions. Moreover, in these highly anisotropic areas, the error is reduced as we pass from Peanut distribution to ODF and, even more, when we consider the VMF distribution. Nevertheless, the use of the VMF distribution would require a preliminary proper estimation of the involved parameters from clinical data, if they are available.

We conclude this section by discussing the computational cost of the three distributions. This cost for the calculation of the fiber distribution functions and the resulting tumor diffusion tensor D_T is almost identical for Peanut distribution and VMF distribution: the construction of D_T via the Peanut distribution does not require any matrix multiplication, while one matrix product is needed for the calculation of D_T in each voxel with the VMF distribution.

The ODF, on the other hand, requires more calculations and, therefore, has a higher computational cost. In fact, for each voxel it requires the numerical approximation of a spherical integral, whose cost depends on the chosen numerical method. Nevertheless, independently from the particular approximation used, the evaluation of the integrand function involves several matrix products and a matrix inversion. We choose the Gauss-Legendre quadrature formula for computing the integral and, in this case, the computational cost for the calculation of D_T in each voxel of the 3D mesh grid is $\mathcal{O}(m^2)$, where m indicates the number of points of the quadrature formula.

4. Numerical simulations

We present 2D simulations of the resulting macroscopic advection-diffusion-reaction Eq. (14). The numerical simulations are performed with a self-developed code in Matlab (MathWorks Inc., Natick, MA). The computational domain is a horizontal brain slice of the left hemisphere, whose reconstruction from MRI data is detailed below. The macroscopic tensor $D_T(x)$ is pre-calculated using the DTI data with the three distribution functions. A Galerkin finite element scheme for the spatial discretization is considered, together with an implicit Euler scheme for the time discretization.

4.1. Reconstruction of the computational domain

We process the brain geometry with the FreeSurfer Software Suite,² an open-source software for the analysis and visualization of structural and functional neuroimaging data from cross-sectional or longitudinal studies. The processing of MRI data with FreeSurfer provides surface and volume information about the two hemispheres of the brain separately, leading to the extraction of a 2D slice that constitutes our computational domain. Examples of the processed outputs are shown in Fig. 5, where both the entire

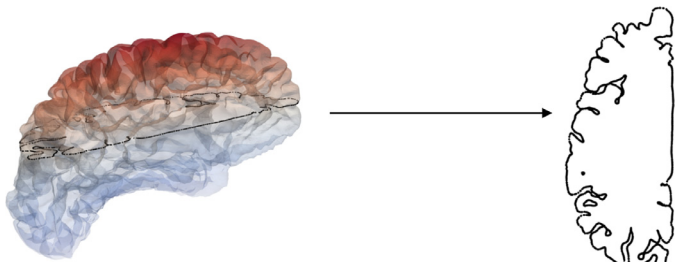


Fig. 5. The left hemisphere visualized with Paraview³ (left); the contour of one slice of the brain (right).

left hemisphere surface and the border of the considered 2D slice are visualized.

The registration between the voxel mesh, given by the DTI dataset, and the brain slice has been obtained with the help of different visualization software programs (Paraview and FSLEyes, the FSL image viewer). The resulting 2D domain has been triangulated with the free mesh generator Gmsh⁴ and the matrices of the finite element approximation have been computed on the resulting grid.

4.2. Coefficient functions and parameters

We choose $Q(x)$, the fraction of insoluble components of ECM interacting at point x with the tumor population and introduced in Section 2.1, to be proportional to the fractional anisotropy of the tissue itself. This approach, introduced in Engwer et al. (2015), is motivated by the fact that the fractional anisotropy is a measure of the alignment of the brain fibers and the function $Q(x)$ should take higher values where the tissue is strongly aligned. Hence, we set

$$Q(x) = FA(D_W(x)). \quad (23)$$

Other possible choices can be considered, like the one introduced in Engwer et al. (2016b) and based on the characteristic diffusion length. A quantitative comparison between different choices of $Q(x)$ is left as future work.

The growth rate $\mu(x, M_0)$ can be also defined in different ways and its choice should be motivated by biological evidence. A logistic term, as well as Gompertzian or exponential growth, can be reasonable choices in the absence of biological data. Following (Jbabdi et al., 2005; Engwer et al., 2016a), we use a logistic growth term, defined as

$$\mu(x, M_0) = c_g \left(1 - \frac{M_0}{C_M} \right) \quad (24)$$

with growth rate c_g and carrying capacity C_M .

For the integrin binding rates and the term describing the natural death of the cells, we refer to Hunt and Surulescu (2017) and we set

$$\begin{aligned} k^+(d_c) &= 0.1 \left(1 + \frac{d_c}{1 + d_c^2} \right) \\ k^-(d_c) &= 0.1 \left(1 + d_c \right) \\ l(M_0) &= c_l M_0. \end{aligned} \quad (25)$$

Observe that the expressions for the attachment and detachment rates are in agreement with the assumption made on the

³ Open-source multiple-platform application for interactive, scientific visualization. Information available at <https://www.paraview.org>.

⁴ Information available at <http://gmsh.info> and, for further details, see also Geuzaine and Remacle (2009).

² Information can be found at <https://surfer.nmr.mgh.harvard.edu/fswiki/FreeSurferWiki> and, for further details, see Fischl (2012) and references therein.

Table 1
Model parameters.

Parameter	Value (units)	Source
s	$0.21 \cdot 10^{-6}$ (ms $^{-1}$)	Chicoine and Silbergeld (1995)
λ_0	0.1 (s $^{-1}$)	Sidani et al. (2007)
λ_1	0.01 (s $^{-1}$)	Engwer et al. (2015)
c_g	$[0.32, 0.72] \times 10^{-5}$ (s $^{-1}$)	Mercapide et al. (2003)
c_l	$[0.32, 0.72] \times 10^{-7}$ (s $^{-1}$)	estimated, based on Engwer et al. (2016b) normalized, based on Engwer et al. (2016a)
C_M	≈ 1	Besserer and Schneider (2015)
α_1	$[0.018, 0.401]$ (Gy $^{-1}$)	Besserer and Schneider (2015)
α_2	$[0.373, 0.389]$ (Gy $^{-1}$)	Besserer and Schneider (2015)
β_1	$[0.023, 0.091]$ (Gy $^{-2}$)	Besserer and Schneider (2015)
β_2	$[0.016, 0.052]$ (Gy $^{-2}$)	Besserer and Schneider (2015)

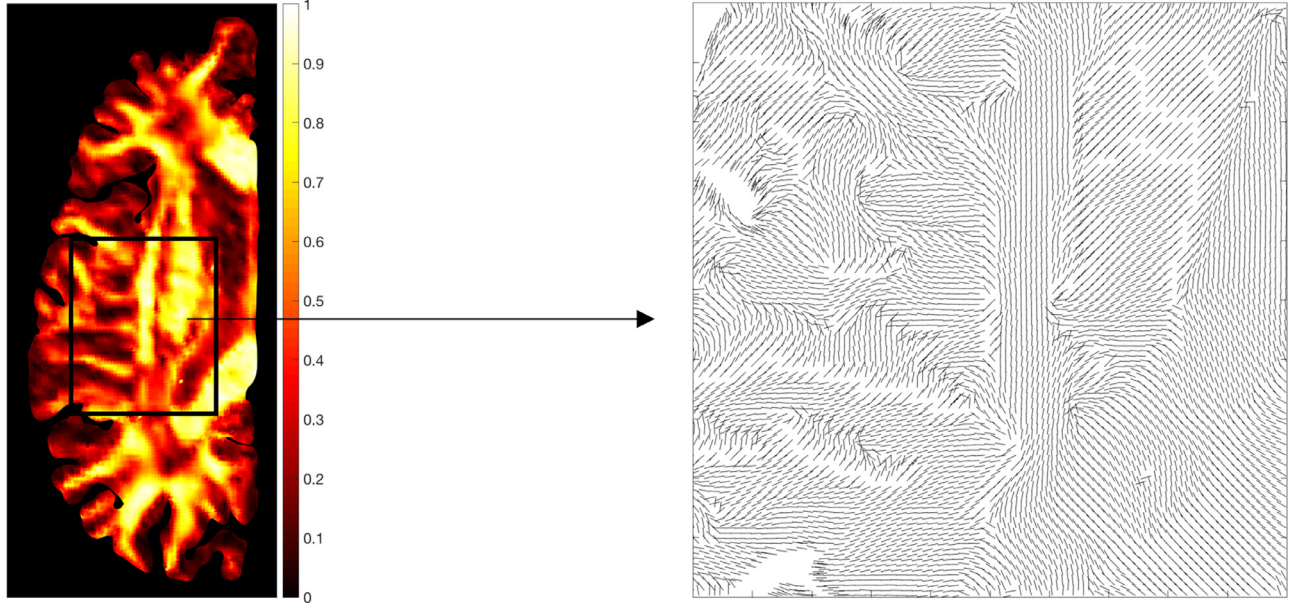


Fig. 6. Fractional anisotropy of $D_W(x)$ (left); visualization of the fiber tracts in a selected subdomain (right).

chemotherapeutic term in Section 2, namely, we consider the function k^+ monotonically decreasing with respect to the given dose d_c , while the function k^- is monotonically increasing with d_c .

In Table 1 we report the range of the values for the remaining parameters involved in the macroscopic Eq. (14), as well as the references they were drawn from. For our simulation purposes, we will use the average values of the indicated intervals.

Finally, in Fig. 6, the values of $FA(D_W(x))$ on the domain and the underlying fiber structure are shown. In particular, the latter, that highly influences tumor dynamics, is visualized on a zoomed region in the center-left, where the leading eigenvector of the tensor $D_W(x)$ is plotted in each point x .

4.3. Results

Considering the parameters given in Table 1, we simulated different scenarios on the domain in Fig. 5. The macroscopic Eq. (14) we consider can be written in the following equivalent form

$$\begin{aligned} \partial_t M_0 - \nabla \nabla : D_T(x) M_0 + \nabla \cdot (g(Q(x)) D_T(x) \nabla Q M_0) \\ = \mu(x, M_0) Q(x) M_0 - L(M_0, R_1) M_0 \end{aligned} \quad (26)$$

with the coefficient functions and parameters introduced in the previous section. The operator $\nabla \nabla :$ is a short form of the full second derivative that, if expanded, gives rise to the Fickian diffusion term plus the additional advection terms (for further details see (Swan et al., 2018; Painter and Hillen, 2013; Engwer et al., 2016a)). A fully-anisotropic advection-diffusion model was

also used in Swan et al. (2018): in fact, this form of advection-diffusion equation is based on cell-movement and, as such, is a more biologically relevant form compared to Fickian diffusion only. We consider homogenous Neumann boundary conditions and an initially constant tumor mass on a small portion of the domain.

We present three sets of numerical results: (A) we consider the model without therapy and we compare the tumor evolution obtained with the three different fiber distribution functions; (B) after selecting one of the distributions, we compare the model output with the results we would obtain without subcellular dynamics, that is by omitting the haptotactic drift term; (C) we add the therapeutic term and simulate its effects on the tumor evolution with the same distribution as in (B).

Fig. 7 shows the comparison in case (A): the tumor evolution over time with the three different fiber distribution functions, in the absence of therapeutic strategy. This model is similar to Engwer et al. (2016a), but with the addition of a term of natural death for the tumor cells. The columns refer to different time instants: the solution is shown after 40 days, 80 days and 120 days. Some similarities can be observed between the tumor dynamics shown in the three rows, especially in qualitative terms. In the three cases, cell displacement inside the tissue covers area of comparable extension and similarly reflects the underlying fiber orientation. Nevertheless, we see that the ODF distribution is able to reproduce anisotropic pattern and branched structures of tumor evolution arising from the underlying tissue structure, contrary to the smoothed effect observed for VMF and Peanut distribution, mainly due, for the latter, to the isotropic component in the tensor D_T (B.2).

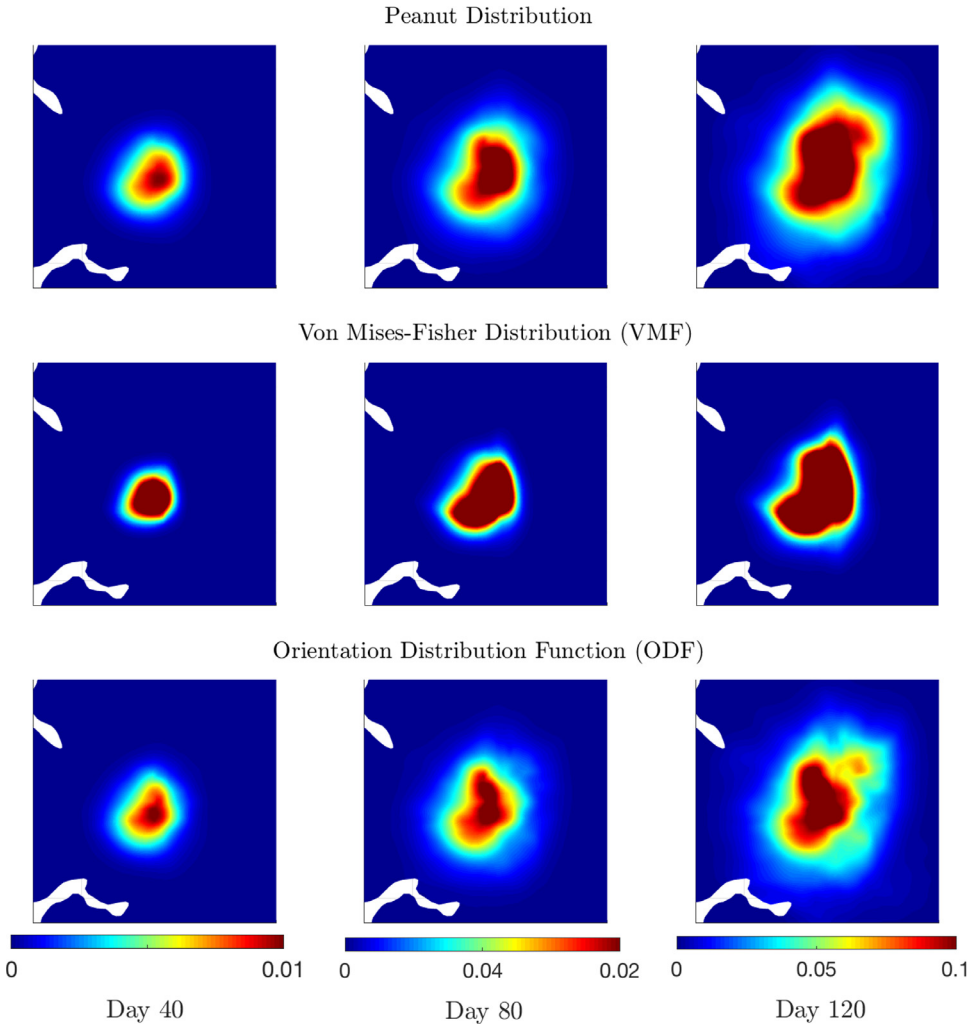


Fig. 7. (A) Simulation of the evolution equation, without therapy, with the three different choices for the fiber distribution function.

For our second set of numerical experiments we then select the ODF for the description of the fiber. In Fig. 8 we illustrate the case (B), the numerical simulations of the tumor evolution with and without the advective term, in the absence of therapy. The advective term originates from the subcellular dynamics and involves also a component related to the divergence of the anisotropic tumor diffusion tensor. Significant anisotropic behaviours, that are evident in the simulations of the model with advection (second row), are not reproduced by the pure diffusive model (first row). In the purely diffusive case, the tumor evolution still shows the influence of the anisotropic diffusion tensor in driving cell movements preferentially along the fiber tracts, but it is not able to reproduce branched patterns and more heterogeneous distribution of the tumor density in the domain. On the other hand, the introduction of the haptotactic drift leads to more branched structures, closer to the ones observed in clinical imaging (e.g., see Zinn et al., 2011; Gerstner et al., 2010). The driven motion of the cells along the tissue structure can be better appreciated in Fig. 9, where the leading eigenvector of the tumor diffusion tensor $D_T(x)$ is also plotted, enhancing the alignment characteristics of the brain tissue and its influence on the tumor dynamics. The diffusion in both cases is anisotropic, due to the presence of tensor $D_T(x)$ in the diffusion term, and along the main fiber tracts it seems to be similarly fast, although slightly faster in the pure diffusion case. However, the cells in the purely diffusive model seem to be slower or less

able to change direction and adapt to the tissue, especially in the region with crossing fiber and at the tumor edges. In summary, Figs. 8 and 9 show that taking subcellular processes into account leads to a non-negligible influence on the spatial distribution of the tumor cells. However, real patient data would be needed to clarify which of the modelling approaches better explains the clinically observed tumor behaviours.

In our third and final set of simulations, we test our model with a therapeutic strategy used in the case of newly diagnosed malignant glioma and based on a combination of chemotherapy and radiotherapy for a period of 6 weeks. Radiotherapy at a dose $d_r = 2$ Gy will be given once per day, 5 days per week from weeks 1 to 6, with a total dose of 60 Gy, while chemotherapeutic agents at a normalized dose of $d_c = 5.0$ (Hunt and Surulescu, 2017) will be administered once per day from weeks 1 to 6. In particular, concerning chemotherapy we concentrate on the reduction of tumor invasion affecting integrin/ECM binding (Stupp and Ruegg, 2007; Desgrange and Cheresh, 2010). Different types of integrin inhibitors, such as cilengitide (targeting $\alpha_v\beta_3|\alpha_v\beta_6$ integrins) or ATN 161 (targeting $\alpha_5\beta_1$ integrins), have been evaluated in preclinical or clinical studies. We consider the action of such chemotherapeutic agents, motivated by different reported trials (e.g., see trials NCT00689221 and NCT01165333 provided at <https://clinicaltrials.gov>). As initial condition for the simulation with therapy, we consider the tumor density obtained from the model without therapy

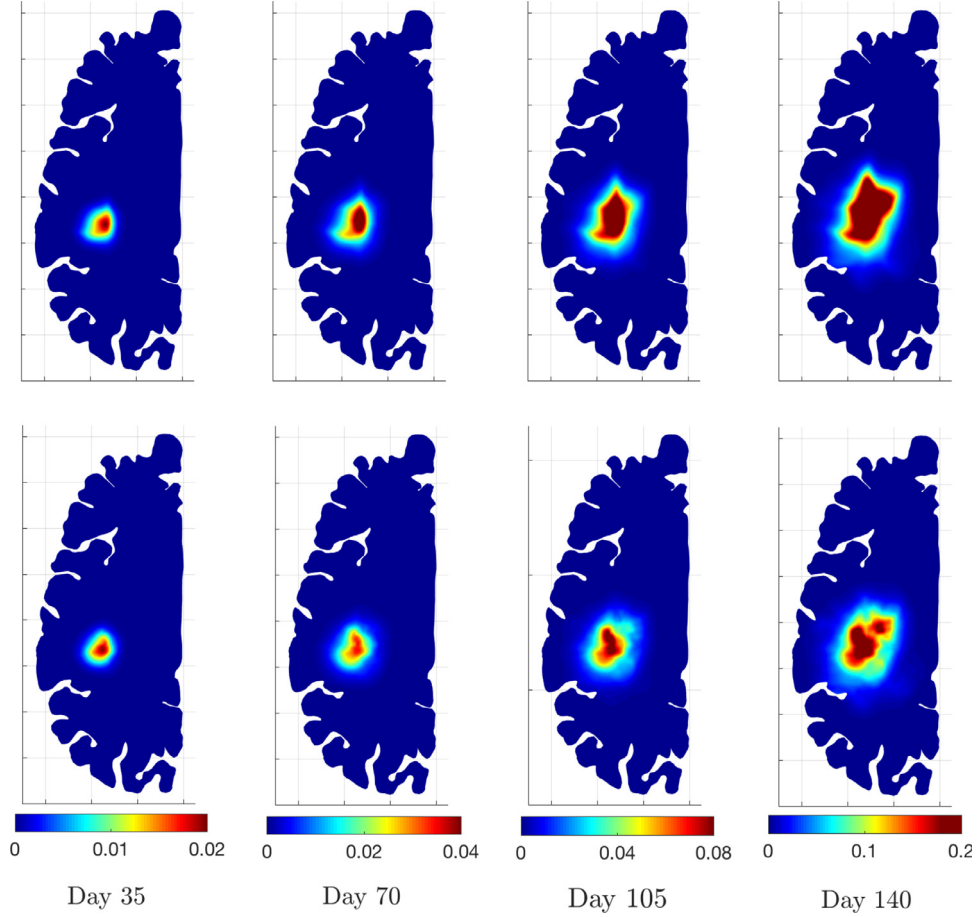


Fig. 8. (B) Simulation of the pure diffusion model (first row) and of the advection-diffusion model (second row) with the ODF for the fiber description.

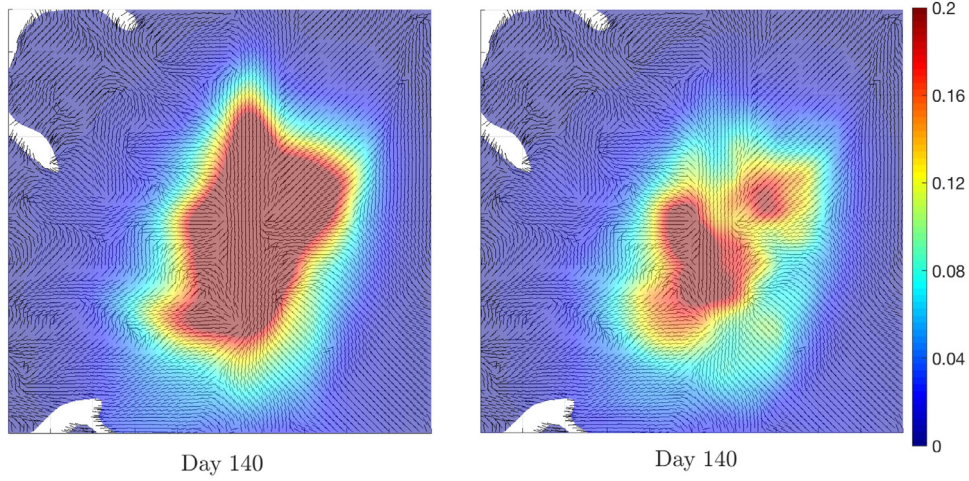


Fig. 9. Tumor evolution after 140 days in the case of the pure diffusion model (left plot) and the advection-diffusion model (right plot), together with the fiber direction.

after 5 weeks. We first observe the effect of the chemotherapy as unique applied strategy, setting the dose $d_r = 0$. Results are shown in Fig. 10 where we plot the difference between the solution for the model without any therapeutic treatment and the one with chemotherapy. In both cases, the tumor diffusion tensor D_T is calculated using the ODF. As chemotherapy does not aim at killing cells, but at reducing their mobility, no changes in the tumor mass are observed. On the other hand, the tumor cells are less invasive

than in the case without therapy, and at the end of the simulation show a larger concentration in the neighbourhood of their initial location. In Fig. 10 also the main fiber direction is shown. We observe that, when chemotherapy is considered, the cells tend to remain clustered in the area of high alignment of the fibers, being less able to change direction and spread inside the brain due to the effect of the therapy on the integrin/ECM binding.

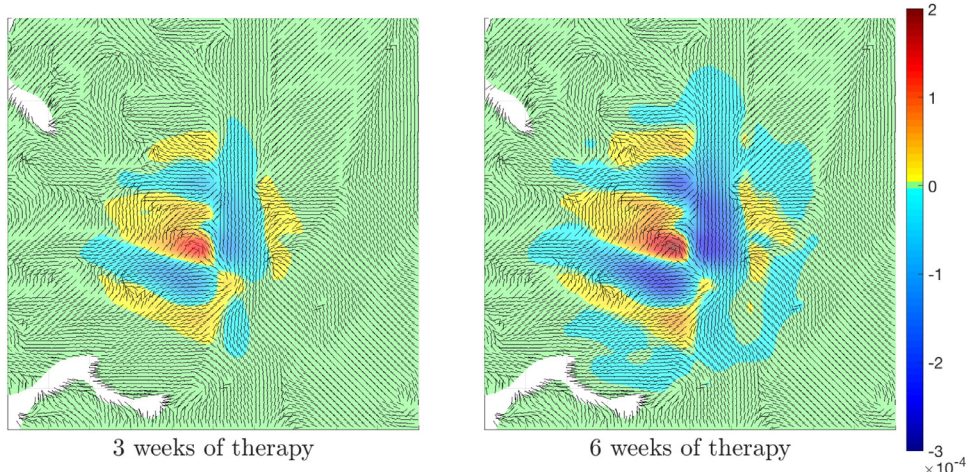


Fig. 10. Difference between the tumor density in the no-therapy model and the density in the case of chemotherapy. This difference is plotted together with the fiber direction. For the construction of D_T we used the ODF .

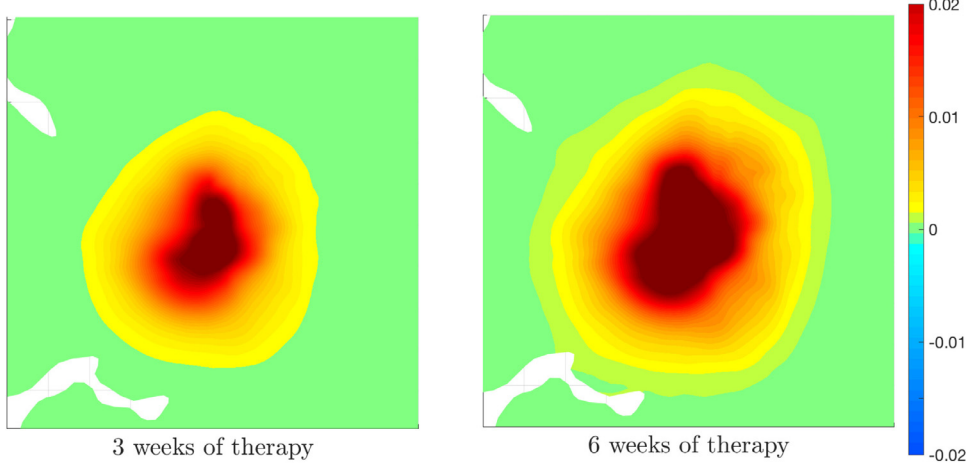


Fig. 11. Difference in the tumor evolution between the no-therapy model and the case in which chemo- and radio-therapy are considered.

Finally, in a similar way we also test the effect of radiotherapy, whose objective is killing cells. The results are shown in Fig. 11, where the difference in the cell density between the model without any therapy and the complete model with both chemo- and radio- therapy is considered. After 6 weeks it is possible to notice a reduction in the tumor density with respect to the situation 3 weeks before (represented by large areas of positive difference). This is particularly evident in those areas where, due to the chemotherapy effects observed in Fig. 10, the cells are more concentrated (i.e., blue areas of Fig. 10).

5. Conclusion and perspectives

In this work we proposed a DTI-based multiscale model aiming to describe the growth, spread and invasion of glioma in the human brain and the effects of a combined treatment of chemo- and radio- therapy on tumor evolution. Starting from previous multiscale modelling approaches (Engwer et al., 2016a; Hunt and Surulescu, 2017), we present a novel formulation that integrates within the same framework the mesoscopic description of tumor proliferation, firstly proposed by Engwer et al. (2016a) and Bellomo2, and a specific therapeutic approach that includes more recent ideas on drugs targeting the inhibition of cell-tissue attachment, as proposed in Hunt and Surulescu (2017). Another original aspect of this work is the extensive focus on the role of the fiber

structure description on the tumor evolution. The macroscopic equation for the tumor cell density (derived from the mesoscale via a parabolic scaling argument), in fact, accounts for real data on the brain structure through the tumor diffusion tensor D_T that depends on a local fiber distribution function $q(x, \theta)$. The way in which the different fiber distribution functions $q(x, \theta)$ translate and reproduce the original DTI information into the simulated model has been largely discussed. The specific capabilities of the three most used fiber distribution functions found in the literature (Peanut, VMF and ODF) are investigated in detail. Their strengths and weaknesses, in terms of both output reliability, biological meaningfulness of the parameters involved and computational cost, have been commented upon in Section 3. After comparing the three distribution functions, we chose ODF (D.2) to proceed with the study of the proposed model, even though the related computational cost and complexity, with respect to the Peanut distribution (19) and the VMF distribution (20), is higher. This choice was motivated by the fact that, based on the shown results, ODF gives an accurate representation of the brain structures in terms of degree of anisotropy of the tissue. However, a proper comparison of the simulated tumor evolution with real patient data would be needed for a complete validation and this will be hopefully matter of future works.

Our simulations show how different choices of the fiber distribution function can influence the results, in terms of extension

of the neoplastic area, shape, tumor infiltration and emergence of heterogenous patterns (see Fig. 8). The role of the fiber in guiding cell movement and glioma invasion clearly emerges, for example in Fig. 9. At the same time, analogously to what observed also in other multiscale modelling formulations (Engwer et al., 2016b; 2015; 2016a), our numerical results highlight the importance of including the microscopic dynamics. In fact, the haptotactic drift term, originating from the introduction of microscopic processes, allows the emergence of more prominent anisotropic behaviour, reflecting what is often clinically observed. Considering different spatio-temporal scales in the model also allows us to include, at various levels in the model formulation, different treatment options, whose effect on tumor invasion and migration in the tissue are clearly shown in Figs. 10 and 11. Upon validation, the availability of a reliable tool to translate the input data into the simulated model, as well as the possibility of extracting from these data realistic information about the computational domain, are key points towards the application of this study on a patient-specific model (Swan et al., 2018; Agosti et al., 2018). Ideally, validation of the results related to the fiber distribution choice could be performed through the comparison of a simulated tumor evolution against longitudinal clinical data following the progression of a tumor in a patient. This remains a future objective, since only data for healthy brain structures were available for this study. The acquisition of the desired data, in fact, presents various difficulties, mainly related to the really poor prognosis of this disease (often discovered already at a late stage of progression).

In this study, we focused on the role of the nervous fibers in facilitating and sustaining glioma invasive spread. Clearly, more complex models, involving several other important factors (such as chemotactic processes, intratumor heterogeneity, evolution of micro-environmental factors) could be formulated, at the probable cost of a more challenging mathematical description and a heavier computational load. A further improvement of the model could be to consider the function $Q(x)$ also depending on time and to include an evolutionary equation for the description of the changes in the healthy tissue structure due to glioma progression. In fact, there is a mutual influence between neoplastic and normal tissue. The ECM structure drives tumor invasion in the brain, but at the same time the tumor degrades the brain ECM through particular enzymes called proteases, in order to make its way inside the tissue. Recent studies (Matías-Román et al., 2005; Mentlein et al., 2012) have shown the possible actions of these enzymes as chemotactic forces, driving the cell movements together with the haptotactic ones. Therefore, the inclusion of such a chemotactic term could give additional insight. Finally, in the same multiscale framework, the use of another scaling (different from the parabolic one) from the mesoscale to the macroscale could be also worth investigating. In this case, we expect a slightly different trend in the tumor evolution with major stress on the role of the advection term, and it would be interesting to observe how the response of the three considered fiber distributions and the therapy effects differ from the results presented here.

Acknowledgments

The authors thank Prof. Luigi Preziosi from Politecnico di Torino (Italy) for his suggestions and helpful discussions that initiated this work. The authors also thank Dr. Marian Gomez Beldarrain from the Department of Neurology at the Galdakao-Usansolo Hospital (Galdakao, Spain) for the DTI data. The authors are grateful to the anonymous referees for their valuable comments, which helped them to considerably improve the paper. Finally, they wish to thank Prof. Christina Surulescu for her useful advices on modelling issues. This research is supported by the Basque Government through the BERC 2018–2021 program and by the Spanish

State Research Agency through BCAM Severo Ochoa excellence accreditation SEV-2017-0718 and through project RTI2018-093416-B-I00 funded by (AEI/FEDER, UE) and acronym MULTICONT. This project has received funding from the European Union's Horizon 2020 research and innovation programme under the Marie Skłodowska-Curie grant agreement No. 713673. The project that gave rise to these results received the support of a fellowship from "la Caixa" Foundation (ID 100010434). The fellowship code is LCF/BQ/IN17/11620056. This work was performed also in the frame of the activities sponsored by the Italian Group of Mathematical Physics (GNFM-INDAM), by the University of Parma (Italy) and by the Italian National Research Project "Multiscale phenomena in Continuum Mechanics: singular limits, off-equilibrium and transitions" (PRIN 2017YBKNC).

Appendix A. Diffusion Anisotropy Indices

Considering a general 3D tensor D , with eigenvalues $\lambda_1 \geq \lambda_2 \geq \lambda_3$ and mean $\bar{\lambda} = \frac{\lambda_1 + \lambda_2 + \lambda_3}{3}$, several scalar indices have been proposed in literature (Painter and Hillen, 2013; Papadakis et al., 1999; Hasan et al., 2004) to characterize its anisotropy. They are called *diffusion anisotropy indices* (DAI) and, among them, we recall:

- *Relative anisotropy*: $RA = \frac{\sqrt{(\lambda_1 - \bar{\lambda})^2 + (\lambda_2 - \bar{\lambda})^2 + (\lambda_3 - \bar{\lambda})^2}}{\sqrt{6\bar{\lambda}}}$,

RA represents the ratio of the anisotropic part of the diffusion tensor to its isotropic part;

- *Fractional anisotropy*: $FA = \sqrt{\frac{3}{2}} \frac{\sqrt{(\lambda_1 - \bar{\lambda})^2 + (\lambda_2 - \bar{\lambda})^2 + (\lambda_3 - \bar{\lambda})^2}}{\sqrt{\lambda_1^2 + \lambda_2^2 + \lambda_3^2}}$,

FA represents the fraction of the magnitude of the diffusion tensor that can be ascribed to anisotropic diffusion;

- *Volume ratio*: $VR = \frac{\lambda_1 \lambda_2 \lambda_3}{\bar{\lambda}^3}$,

VR represents the ratio of the ellipsoid volume to the volume of a sphere of radius $\bar{\lambda}$.

These three indices are characterized by rotational invariance (there is no bias due to fiber orientation in estimating the anisotropy) and symmetry respect to the three principal diffusivities (sorting-independency and less sensitivity to extraneous noise). Different studies (Papadakis et al., 1999; Hasan et al., 2004; Kingsley and Monahan, 2005) have shown that there are significant differences between these three indices, especially in terms of sensitivity to anisotropy, contrast between low and high anisotropy areas and contrast-to-noise ratio. However, these differences are not so strong, especially for small anisotropy variation, to justify an intrinsic advantage of one index on the others. In particular, FA seems to provide the most detailed representation of the anisotropy characterizing the tissue; it reveals well the various anisotropic structures, even for areas of mild and low anisotropy, providing good anatomical details of the anisotropic regions, although it has an increasing noise in the area of low anisotropy.

Appendix B. Peanut distribution

Firstly introduced by Painter and Hillen in Painter and Hillen (2013), the definition of the Peanut distribution is related to the concept of apparent diffusion coefficient (ADC). It is defined, generally, by taking the ratio of the mean-squared displacement measured along a particular direction and the diffusion time of the experiment.

In the specific case of a simple model for anisotropic diffusion, described by a diffusion tensor D , the mean-squared displacement along a given direction $\theta \in \mathbb{S}^{n-1}$ is given by $\sigma_\theta^2 = 2t\theta^T D \theta$, where t is the diffusion time. So, ADC in the direction θ is given by the

following expression (Basser, 2008)

$$ADC_\theta := \frac{\sigma_\theta^2}{2t} = \theta^T D \theta.$$

Since ADC is an indicator of the anisotropy of the tissue, a possible choice for the construction of the fiber distribution function is to assume that the cell turning is directly correlated to it. As a consequence, the Peanut distribution function for the fiber orientation description takes the following form:

$$q(x, \theta) = \frac{n}{|\mathbb{S}^{n-1}| \operatorname{Tr}(D_W(x))} \theta^T D_W(x) \theta. \quad (\text{B.1})$$

Following Lemma 1 in Painter and Hillen (2013) it is possible to get the general expression for the tumor diffusion tensor $D_T(x)$ in n dimension, starting from the relation (15):

$$D_T(x) = \frac{s^2}{(n+2)\lambda_0} \left(\mathbb{I} + \frac{2}{\operatorname{Tr}(D_W)} D_W \right). \quad (\text{B.2})$$

This expression reveals the direct link between the original tensor D_W and the macroscopic diffusion tensor D_T , presenting an isotropic component proportional to \mathbb{I} and an anisotropic component proportional to D_W . So, theoretically, even in the case of completely anisotropic environment, D_T will always present an isotropic part, leading to a partial loss of data information.

Appendix C. Von Mises-Fisher Distribution

The Von Mises-Fisher (VMF) distribution is one of the most useful distribution for spherical data from the standpoint of the statistical inference, as largely explained in Mardia and Jupp (2009). The most general expression of this distribution for data $\hat{x} \in \mathbb{S}^{n-1}$ results in a probability density function of this form:

$$f(\hat{x}, \mu, \kappa) = \left(\frac{\kappa}{2} \right)^{\frac{n}{2}-1} \frac{1}{\Gamma(\frac{n}{2}) I_{\frac{n}{2}-1}} \exp\{\kappa \mu^T \hat{x}\}$$

where $\kappa \geq 0$ is the concentration parameter, μ is the mean direction, with norm one, I_v is the modified Bessel function of the first kind and of order v and Γ is the Gamma function. This distribution, for $\kappa > 0$, has a mode at the mean direction and, the larger the value of the concentration parameter, the greater the clustering around this direction.

The special cases which we are interested in are defined for $n = 2$ (planar case) and $n = 3$ (spherical case). Consider the following representation of the space-dependent water diffusion tensor $D_W(x)$:

$$D_W(x) = \sum_{i=1}^n \lambda_i(x) \phi_i(x) \phi_i(x)^T$$

with λ_i and ϕ_i ($i = 1 \dots n$) being the eigenvalues and corresponding eigenvectors of the tensor, respectively orthogonal and normalized due to its symmetry; in particular, the eigenvectors denote the axis of dominating anisotropy and the eigenvalues the degree of anisotropy.

With this notation, for the planar case, the dominant direction μ for the movement is given by the leading eigenvector of D_W , because it is natural to consider that the turning is concentrated in the dominant direction of anisotropy (Painter and Hillen, 2013). Additionally, two other requirements are considered for building the well-known and used expression introduced in Painter and Hillen (2013). Firstly a constant parameter $\delta \in [0, 1]$, describing an inherent degree of randomized turning, is added for partially controlling the size of the resulting isotropic component of D_T . Then the concentration parameter κ is substituted by a function $k(x)$ for the concentration level that should increase along the direction of greater anisotropy. For this reason, a possible choice for $k(x)$ consists in considering it proportional to the fractional anisotropy of D_W through a concentration factor κ , describing the sensitivity of the cells to the directional information given by the environment, i.e., $k(x) = \kappa FA(D_W(x))$. Thus, considering a bimodal form of the VMF distribution, the expression for the fiber distribution function results:

$$q(x, \theta) = \frac{\delta}{2\pi} + (1-\delta) \frac{1}{4\pi I_0(k)} \left(e^{k(x)\phi_1 \cdot \theta} + e^{-k(x)\phi_1 \cdot \theta} \right). \quad (\text{C.1})$$

Considering (15) and (C.1), the expression of $D_T(x)$ for $n = 2$, as explicitly calculated into (Hillen and Painter, 2013), is given by:

$$D_T(x) = \frac{s^2}{2\lambda_0} \left(\left(\delta + (1-\delta) \left(1 - \frac{I_2(k(x))}{I_0(k(x))} \right) \right) \mathbb{I} + 2(1-\delta) \frac{I_2(k(x))}{I_0(k(x))} \phi_1(x) \phi_1(x)^T \right). \quad (\text{C.2})$$

In particular, we observe that the parameter δ plays the role of weight for the isotropic and the anisotropic component of D_T , determining the relevance of each part; analogous role is played by the function $k(x)$. If $\delta = 1$, D_T simply describes a complete isotropic environment. The same happens when $k(x) = 0$, since in this case the ratio $\frac{I_2(k(x))}{I_0(k(x))} = 0$. In particular, $k(x) = 0$ occurs either in the case of isotropic DTI data, i.e., $FA(D_W) = 0$, or in the case of cells not responding to the environmental anisotropy, i.e., $\kappa = 0$. On the contrary, when the value of $k(x)$ grows or the value of δ is close to zero, the anisotropic part gains more importance.

Unlike in the Peanut distribution case, it is possible here to have bigger control on the fiber density trend changing δ and κ . On one

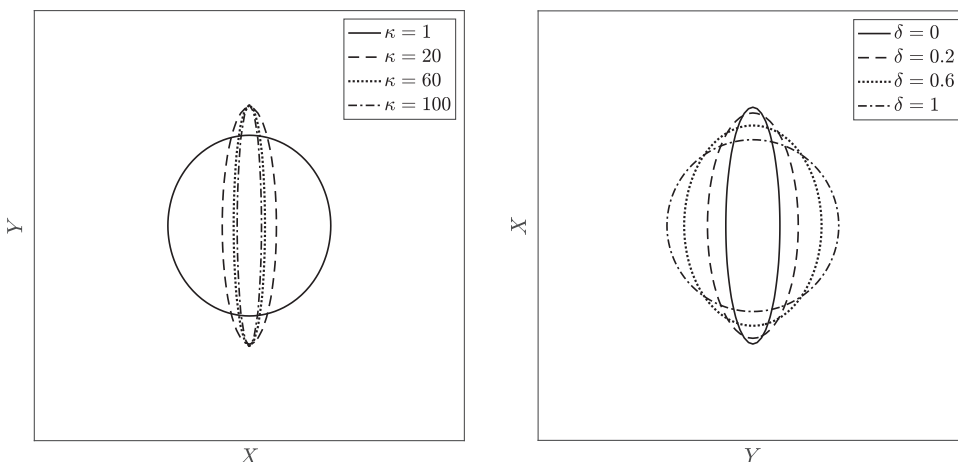


Fig. C.12. $D_T(x)$ for VMF Distribution varying κ (left) and δ (right).

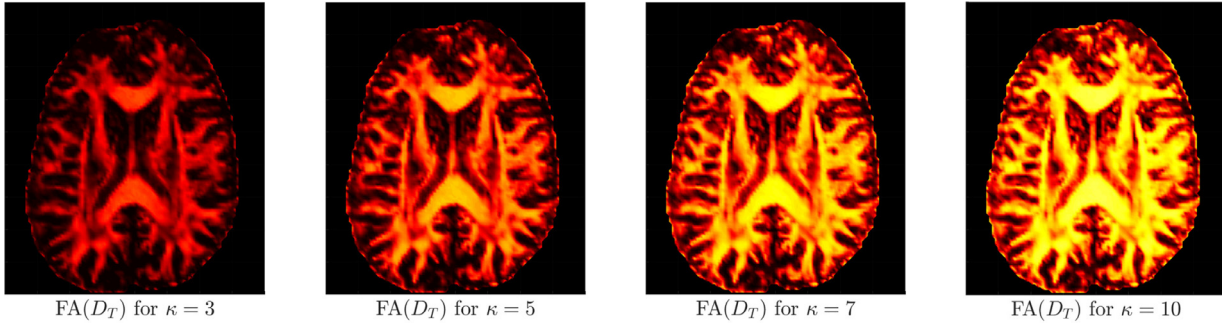


Fig. C.13. FA(D_T) for different values of κ and δ fixed to 0.05.

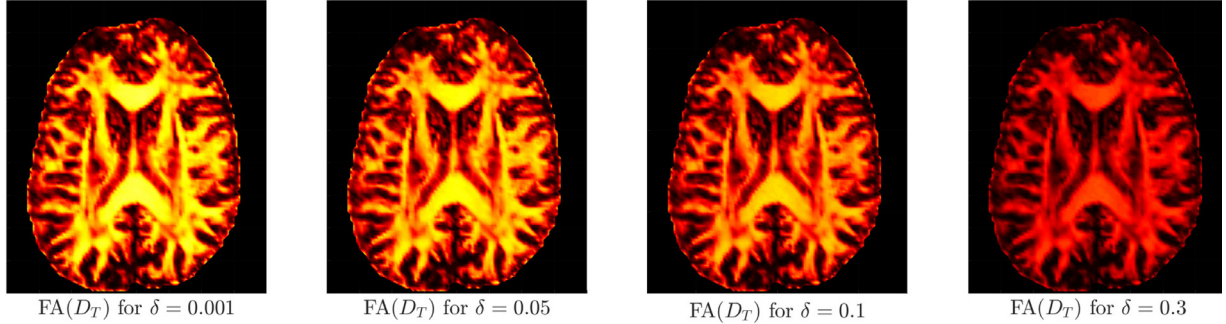


Fig. C.14. FA(D_T) for different values of δ and κ fixed to 7.

side, this means that D_T may be calibrated in order to be as similar as possible to the tensor D_W , but on the other hand this makes it strongly dependent on the parameters κ and δ , whose meaning and identification are not so clear. In fact, although it seems reasonable to choose them by fitting the original data, their biological interpretation and estimation remain still uncertain: as a consequence, the reliability of the results may be compromised. In particular, we compare the effect on $FA(D_T)$ of parameters κ and δ . The results are shown in Fig. C.12 for the single point case and in Figs. C.13 and C.14 for a brain slice.

Due to the difficulty to obtain clinical data for the evolution of a glioma in the brain, for the parameter δ we consider, for the comparison and the simulations, the value proposed in Painter and Hillen (2013), i.e., $\delta = 0.05$. On the other hand, for the estimation of the parameter κ , different tuning procedures are possible (e.g., see Swan et al., 2018). We consider a least square optimization to fit the data related to the FA of our D_W tensor with the resulting FA of the tensor D_T given by (C.2). In particular, the optimization procedure provides a value of $\kappa = 5.775$, which minimizes the norm of the residual

$$\|FA(D_T) - FA(D_W)\|_2 = \sqrt{\sum_{i=1}^N (FA(D_T)_i - FA(D_W)_i)^2}. \quad (\text{C.3})$$

Note that N is the number of data points. The same optimization tool has been used in the 1D case shown in Fig. 1 to estimate the parameter κ for the single data point chosen as example. In particular, in that case, it gives $\kappa = 46$.

Extending the analysis to the $n = 3$ case, following (Painter and Hillen, 2013), we consider the bimodal form of the distribution combined with a uniform distribution depending on the parameter $\delta \in [0, 1]$. The fiber configuration in this case is described by:

$$q(x, \theta) = \frac{\delta}{4\pi} + (1 - \delta) \frac{k(x)}{4\pi \sinh k(x)} (\cosh(k(x)\phi_1 \cdot \theta)). \quad (\text{C.4})$$

The direct calculation of the tumor diffusion tensor expression provides:

$$D_T(x) = \frac{s^2}{3\lambda_0} \left[\left(\delta + (1 - \delta) \left(\frac{\coth k(x)}{k(x)} - \frac{1}{k(x)^2} \right) \right) \mathbb{I} + (1 - \delta) \left(1 - \frac{3 \coth k(x)}{k(x)} + \frac{3}{k(x)^2} \right) \phi_1(x) \phi_1(x)^T \right]. \quad (\text{C.5})$$

Appendix D. Orientation Distribution Function

A third approach is based on the concept of the Orientation Distribution Function, simply indicated as ODF. The 3D probability density function (PDF) of diffusion $\mathcal{P}(x, \hat{v})d\Omega$ gives the displacement probability for a molecule in the point x to be located inside a fiber bundle passing in the direction \hat{v} through the infinitesimal solid angle $d\Omega$, providing helpful information in the study of the tissue microstructure. The ODF, instead, represent the marginal probability of diffusion in a given direction and it is fundamental for mapping the orientation architecture of the tissue (Aganj et al., 2010; 2011).

Considering the standard spherical coordinates system and assuming that the PDF of diffusion is a symmetric function $\mathcal{P}(\vec{r}) = \mathcal{P}(-\vec{r})$, the probability of diffusion in a direction \hat{v} through the solid angle $d\Omega$ is computed by integrating the displacement probabilities for all magnitude r , keeping the direction constant, i.e.,

$$ODF(\hat{v}) = \int_0^\infty \mathcal{P}(r\hat{v}) r^2 dr. \quad (\text{D.1})$$

The application of this distribution to fiber orientation analysis comes from some experimental results that show the correspondence between the peaks of the ODF and the principal directions of the underlying fibers (Perrin et al., 2005). In particular a non-linear, monotonically increasing relationship between the FA of generated diffusion tensor related to an underlying fiber and the mean principal curvature of the ODF at the principal direction of the fiber itself is shown in Bloy and Verma (2008).

In the case of Diffusion Tensor Imaging (Aganj et al., 2011), the probability density function of diffusion is given by the standard 3D Gaussian PDF:

$$\mathcal{P}(\mathbf{r}\hat{\nu}) = \frac{1}{(2\pi)^{\frac{3}{2}} |D|^{\frac{1}{2}}} e^{-\frac{1}{2} \mathbf{r}\hat{\nu}^T D^{-1} \mathbf{r}\hat{\nu}}$$

with D proportional to the estimated diffusion tensor and $|D|$ denoting the determinant of this tensor. Inserting this expression in (D.1), we obtain:

$$ODF(\hat{\nu}) = \frac{1}{4\pi |D|^{\frac{1}{2}} (\hat{\nu}^T (D)^{-1} \hat{\nu})^{\frac{3}{2}}}.$$

Thus, setting the fiber orientation density $q(x, \theta)$ equal to ODF, setting the direction θ equal to the direction $\hat{\nu}$ and considering the water diffusion tensor D_W as original estimated tensor, we obtain:

$$q(x, \theta) = \frac{1}{4\pi |D_W(x)|^{\frac{1}{2}} (\theta^T (D_W(x))^{-1} \theta)^{\frac{3}{2}}}. \quad (\text{D.2})$$

In this case, we do not have an explicit expression for the tumor diffusion tensor D_T , but we consider its integral formulation (15) and we approximate it numerically.

References

- Aganj, I., Lenglet, C., Jahanshad, N., Yacoub, E., Harel, N., Thompson, P.M., Sapiro, G., 2011. A hough transform global probabilistic approach to multiple-subject diffusion MRI tractography. *Med. Image. Anal.* 15 (4), 414–425.
- Aganj, I., Lenglet, C., Sapiro, G., Yacoub, E., Ugurbil, K., Harel, N., 2010. Reconstruction of the orientation distribution function in single and multiple shell qball imaging within constant solid angle. *Magn. Reson. Med.* 64 (2), 554–566.
- Agosti, A., Cattaneo, C., Giverso, C., Ambrosi, D., Ciarletta, P., 2018. A computational framework for the personalized clinical treatment of glioblastoma multiforme. *J. Appl. Math. Mech.* 98 (12), 2307–2327.
- Alfonso, J.C.L., Talkenberger, K., Seifert, M., Klink, B., Hawkins-Daarud, A., Swanson, K.R., Hatzikirou, H., Deutsch, A., 2017. The biology and mathematical modelling of glioma invasion: a review. *J. Royal Soc. Interface* 14 (136), 20170490.
- Ambrosi, D., Preziosi, L., 2002. On the closure of mass balance models for tumor growth. *Math. Mod. Meth. Appl. S.* 12 (05), 737–754.
- Anderson, A.R., Chaplain, M.A., Newman, E.L., Steele, R.J., Thompson, A.M., 2000. Mathematical modelling of tumour invasion and metastasis. *Comput. Math. Method.* M. 2 (2), 129–154.
- Barcas, V.H., Tranquillo, R.T., 1997. An anisotropic biphasic theory of tissue-equivalent mechanics: the interplay among cell traction, fibrillar network deformation, fibril alignment, and cell contact guidance. *J. Biomech. Eng.* 119 (2), 137–145.
- Basser, P.J., 2008. Diffusion and diffusion tensor MR imaging: fundamentals. In: *Magnetic Resonance Imaging of the Brain and Spine*. Lippincott Williams, pp. 1752–1767.
- Bellomo, N., Bellouquid, A., Nieto, J., Soler, J., 2010. Complexity and mathematical tools toward the modelling of multicellular growing systems. *Math. Comput. Model.* 51 (5–6), 441–451.
- Bellomo, N., Bellouquid, A., Nieto, J., Soler, J., 2012. On the asymptotic theory from microscopic to macroscopic growing tissue models: an overview with perspectives. *Math. Mod. Meth. Appl. S.* 22 (01), 1130001.
- Besserer, J., Schneider, U., 2015. Track-event theory of cell survival with second-order repair. *Radiat. Environ. Biophys.* 54 (2), 167–174.
- Bitouni, V., Trucu, D., Chaplain, M.A., Eftimie, R., 2018. Aggregation and travelling wave dynamics in a two-population model of cancer cell growth and invasion. *Math. Med. Biol.* 35 (4), 541–577.
- Bloy, L., Verma, R., 2008. On computing the underlying fiber directions from the diffusion orientation distribution function. In: *Medical Image Computing and Computer-Assisted Intervention*. Springer, pp. 1–8.
- Bondiau, P.Y., Clatz, O., Sermesant, M., Marcy, P.Y., Delingette, H., Frenay, M., Ayache, N., 2008. Biocomputing: numerical simulation of glioblastoma growth using diffusion tensor imaging. *Phys. Med. Biol.* 53 (4), 879.
- Borcherding, R.K., McKinley, S.A., 2018. Continuum approximation of invasion probabilities. *Multiscale Model. Sim.* 16 (2), 551–582.
- Böttger, K., Hatzikirou, H., Chauviere, A., Deutsch, A., 2012. Investigation of the migration/proliferation dichotomy and its impact on avascular glioma invasion. *Math. Model. Nat. Pheno.* 7 (1), 105–135.
- Brenner, D.J., 2008. The linear-quadratic model is an appropriate methodology for determining isoeffective doses at large doses per fraction. *Semin. Radiat. Oncol.* 18 (4), 234–239.
- Byrne, H.M., 2010. Dissecting cancer through mathematics: from the cell to the animal model. *Nat. Rev. Cancer* 10 (3), 221.
- Chaplain, M.A., Lolas, G., 2006. Mathematical modelling of cancer invasion of tissue: dynamic heterogeneity. *Netw. Heterog. Media* 1 (3), 399–439.
- Chauviere, A., Hillen, T., Preziosi, L., 2007. Modeling cell movement in anisotropic and heterogeneous network tissues. *Netw. Heterog. Media* 2 (2), 333.
- Chicoine, M.R., Silbergeld, D.L., 1995. Assessment of brain tumor cell motility in vivo and in vitro. *J. Neurosurg.* 82 (4), 615–622.
- Clatz, O., Sermesant, M., Bondiau, P.Y., Delingette, H., Warfield, S.K., Malandain, G., Ayache, N., 2005. Realistic simulation of the 3-D growth of brain tumors in MR images coupling diffusion with biomechanical deformation. *IEEE T. Med. Imaging* 24 (10), 1334–1346.
- Cobzas, D., Mosayebi, P., Murtha, A., Jagersand, M., 2009. Tumor invasion margin on the riemannian space of brain fibers. In: *Medical Image Computing and Computer-Assisted Intervention*. Springer, pp. 531–539.
- Colombo, M.C., Giverso, C., Faggiano, E., Boffano, C., Acerbi, F., Ciarletta, P., 2015. Towards the personalized treatment of glioblastoma: integrating patient-specific clinical data in a continuous mechanical model. *PLoS One* 10 (7), e0132887.
- Corbin, G., Hunt, A., Klar, A., Schneider, F., Surulescu, C., 2018. Higher-order models for glioma invasion: from a two-scale description to effective equations for mass density and momentum. *Math. Mod. Meth. Appl. S.* 28 (09), 1771–1800.
- Demuth, T., Berens, M.E., 2004. Molecular mechanisms of glioma cell migration and invasion. *J. Neuro-oncol.* 70 (2), 217–228.
- Desgranges, J.S., Cheresh, D.A., 2010. Integrins in cancer: biological implications and therapeutic opportunities. *Nat. Rev. Cancer* 10 (1), 9–22.
- Engwer, C., Hillen, T., Knappitsch, M., Surulescu, C., 2015. Glioma follow white matter tracts: a multiscale DTI-based model. *J. Math. Biol.* 71 (3), 551–582.
- Engwer, C., Hunt, A., Surulescu, C., 2016. Effective equations for anisotropic glioma spread with proliferation: a multiscale approach and comparisons with previous settings. *Math. Med. Biol.* 33 (4), 435–459.
- Engwer, C., Knappitsch, M., Surulescu, C., 2016. A multiscale model for glioma spread including cell-tissue interactions and proliferation. *Math. Biosci. Eng.* 13 (2), 443–460.
- Fangliang, D., 2012. Maximum principle and application of parabolic partial differential equations. *IERI Procedia* 3, 198–205.
- Fischl, B., 2012. Freesurfer. *Neuroimage* 62 (2), 774–781.
- Fowler, J.F., 1989. The linear-quadratic formula and progress in fractionated radiotherapy. *Brit. J. Radiol.* 62 (740), 679–694.
- Frieboes, H.B., Lowengrub, J.S., Wise, S., Zheng, X., Macklin, P., Bearer, E.L., Cristini, V., 2007. Computer simulation of glioma growth and morphology. *Neuroimage* 37, S59–S70.
- Gritsenko, P., Ilina, O., Friedl, P., 2012. Interstitial guidance of cancer invasion. *J. Pathol.* 226 (2), 185–199.
- Gerstner, E.R., Chen, P.J., Wen, P.Y., Jain, R.K., Batchelor, T.T., Sorensen, G., 2010. Infiltrative patterns of glioblastoma spread detected via diffusion MRI after treatment with cediranib. *Neuro-oncology* 12 (5), 466–472.
- Geuzaine, C., Remacle, J.F., 2009. Gmsh: a 3D finite element mesh generator with built-in pre and post processing facilities. *Int. J. Numer. Meth. Eng.* 79 (11), 1309–1331.
- Gevertz, J.L., Torquato, S., 2006. Modeling the effects of vasculature evolution on early brain tumor growth. *J. Theo. Biol.* 243 (4), 517–531.
- Giese, A., Bjerkvig, R., Behrens, M.E., Westphal, M., 2003. Cost of migration: invasion of malignant gliomas and implications for treatment. *J. Clin. Oncol.* 21 (8), 1624–1636.
- Giovanna, M.D., Kaye, A.H., 2007. Integrins: molecular determinants of glioma invasion. *J. Clin. Neurosci.* 14 (11), 1041–1048.
- Hasan, K.M., Alexander, A.L., Narayan, P.A., 2004. Does fractional anisotropy have better noise immunity characteristics than relative anisotropy in diffusion tensor MRI? an analytical approach. *Magn. Reson. Med.* 51 (2), 413–417.
- Hatzikirou, H., Basanta, D., Simon, M., Schaller, K., Deutsch, A., 2012. ‘Go or grow’: the key to the emergence of invasion in tumour progression? *Math. Med. Biol.* 29 (1), 49–65.
- Hatzikirou, H., Deutsch, A., Schaller, C., Simon, M., Swanson, K., 2005. Mathematical modelling of glioblastoma tumour development: a review. *Math. Mod. Meth. Appl. S.* 15 (11), 1779–1794.
- Hillen, T., 2006. M^5 mesoscopic and macroscopic models for mesenchymal motion. *J. Math. Biol.* 53 (4), 585–616.
- Hillen, T., Painter, K.J., 2013. Transport and anisotropic diffusion models for movement in oriented habitats. In: *Dispersal, Individual Movement and Spatial Ecology*. Springer, pp. 177–222.
- Hunt, A., Surulescu, C., 2017. A multiscale modeling approach to glioma invasion with therapy. *Vietnam J. Math.* 45 (1–2), 221–240.
- Huttenlocher, A., Horwitz, A.R., 2011. Integrins in cell migration. *CSH Perspect. Biol.* 3 (9), a005074.
- Jbabdi, S., Mandonnet, E., Duffau, H., Capelle, L., Swanson, K.R., Péligrini-Issac, M., Guillemin, R., Benali, H., 2005. Simulation of anisotropic growth of low grade gliomas using diffusion tensor imaging. *Magn. Reson. Med.* 54 (3), 616–624.
- Jenkinson, M., Beckmann, C.F., Behrens, T.E., Woolrich, M.W., Smith, S.M., 2012. *Fsl*. *Neuroimage* 62 (2), 782–790.
- Kelkel, J., Surulescu, C., 2012. A multiscale approach to cell migration in tissue networks. *Math. Mod. Meth. Appl. S.* 22 (03), 1150017.
- Khajanchi, S., 2019. Stability analysis of a mathematical model for glioma-immune interaction under optimal therapy. *Int. J. Nonlin. Sci. Num.* 20 (3–4), 269–285.
- Khajanchi, S., Nieto, J.J., 2019. Mathematical modeling of tumor-immune competitive system, considering the role of time delay. *Appl. Math. Comput.* 340, 180–205.
- Kim, Y., Roh, S., 2013. A hybrid model for cell proliferation and migration in glioblastoma. *Discrete Cont. Dyn. - B* 18 (4), 969–1015.
- Kingsley, P.B., Monahan, W.G., 2005. Contrast to noise ratios of diffusion anisotropy indices. *Magn. Reson. Med.* 53 (4), 911–918.
- Konukoglu, E., Clatz, O., Bondiau, P.Y., Delingette, H., Ayache, N., 2010. Extrapolating glioma invasion margin in brain magnetic resonance images: suggesting new irradiation margins. *Med. Image Anal.* 14 (2), 111–125.

- Lefrank, F., Brotchi, J., Kiss, R., 2005. Possible future issues in the treatment of glioblastomas: special emphasis on cell migration and the resistance of migrating glioblastoma cells to apoptosis. *J. Clin. Oncol.* 23 (10), 2411–2422.
- Lorenz, I., Surulescu, C., 2014. On a class of multiscale cancer cell migration models: well-posedness in less regular function spaces. *Math. Mod. Meth. Appl. S.* 24 (12), 2383–2436.
- Maini, P.K., 1989. Spatial and spatio-temporal patterns in a cell-haptotaxis model. *J. Math. Biol.* 27 (5), 507–522.
- Mardia, K.V., Jupp, P.E., 2009. Directional Statistics, Vol. 494. John Wiley & Sons.
- Martirosyan, N.L., Rutter, E.M., Ramey, W.L., Kostelich, E.J., Kuang, Y., Preul, M.C., 2015. Mathematically modeling the biological properties of gliomas: a review. *Math. Biosci. Eng.* 12 (4), 879–905.
- Matías-Román, S., Gálvez, B.G., Genís, L., Yáñez Mó, M., de la Rosa, G., Sánchez-Mateos, P., Sánchez-Madrid, F., Arroyo, A.G., 2005. Membrane type 1-matrix metalloproteinase is involved in migration of human monocytes and is regulated through their interaction with fibronectin or endothelium. *Blood* 105 (10), 3956–3964.
- Mentlein, R., Hattermann, K., Held-Feindt, J., 2012. Lost in disruption: role of proteases in glioma invasion and progression. *Biochim. Biophys. Acta, Rev. Cancer* 1825 (2), 178–185.
- Meral, G., Stinner, C., Surulescu, C., 2015. On a multiscale model involving cell contractility and its effects on tumor invasion. *Discrete Cont. Dyn. - B* 20 (1), 189–213.
- Mercapide, J., Lopez De Cicco, R., Castresana, J.S., Klein-Szanto, A.J., 2003. Stromelysin-1/matrix metalloproteinase-3 (MMP-3) expression accounts for invasive properties of human astrocytoma cell lines. *Int. J. Cancer.* 106 (5), 676–682.
- Othmer, H.G., Hillen, T., 2000. The diffusion limit of transport equations derived from velocity-jump processes. *SIAM J. Appl. Math.* 61 (3), 751–775.
- Painter, K.J., Hillen, T., 2013. Mathematical modelling of glioma growth: the use of diffusion tensor imaging (DTI) data to predict the anisotropic pathways of cancer invasion. *J. Theor. Biol.* 323, 25–39.
- Papadakis, N.G., Xing, D., Houston, G.C., Smith, J.M., Smith, M.I., James, M.F., Parsons, A.A., Huang, C.L.H., Hall, L.D., Carpenter, T.A., 1999. A study of rotationally invariant and symmetric indices of diffusion anisotropy. *Magn. Reson. Imaging* 17 (6), 881–892.
- Perrin, M., Poupon, C., Rieul, B., Leroux, P., Constantinesco, A., Mangin, J.F., LeBihan, D., 2005. Validation of q-ball imaging with a diffusion fibre-crossing phantom on a clinical scanner. *Philos. Trans. Royal Soc. Lond. B Biol. Sci.* 360 (1457), 881–891.
- Rockne, R., Alvord, E.C., Rockhill, J.K., Swanson, K.R., 2009. A mathematical model for brain tumor response to radiation therapy. *J. Math. Biol.* 58 (4–5), 561.
- Ruzicka, M., 2006. Nichtlineare Funktionalanalysis: Eine Einführung. Springer-Verlag.
- Sachs, R.K., Hlatky, L.R., Hahnfeldt, P., 2001. Simple ODE models of tumor growth and anti-angiogenic or radiation treatment. *Math. Comput. Model.* 33 (12–13), 1297–1305.
- Showalter, R.E., 2013. Monotone operators in Banach space and nonlinear partial differential equations, Vol. 49. American Mathematical Soc.
- Sidani, M., Wessels, D., Mouneimne, G., Ghosh, M., Goswami, S., Sarmiento, C., Wang, W., Kuhl, S., El-Sibai, M., Backer, J.M., Eddy, R., 2007. Cofilin determines the migration behavior and turning frequency of metastatic cancer cells. *J. Cell Biol.* 179 (4), 777–791.
- Stinner, C., Surulescu, C., Winkler, M., 2014. Global weak solutions in a PDE-ODE system modeling multiscale cancer cell invasion. *SIAM J. Math. Anal.* 46 (3), 1969–2007.
- Stupp, R., Ruegg, C., 2007. Integrin inhibitors reaching the clinic. *J. Clin. Oncol.* 25, 1637–1638.
- Sun, S., Titushkin, I., Cho, M., 2006. Regulation of mesenchymal stem cell adhesion and orientation in 3D collagen scaffold by electrical stimulus. *Bioelectrochemistry* 69 (2), 133–141.
- Swan, A., Hillen, T., Bowman, J.C., Murtha, A.D., 2018. A patient-specific anisotropic diffusion model for brain tumour spread. *B. Math. Biol.* 80 (5), 1259–1291.
- Swanson, K.R., Alvord, E.C., 2000. A quantitative model for differential motility of gliomas in grey and white matter. *Cell Proliferat.* 33 (5), 317–329.
- Swanson, K.R., Alvord, E.C., 2003. Virtual resection of gliomas: effect of extent of resection on recurrence. *Math. Comput. Model.* 37 (11), 1177–1190.
- Swanson, K.R., Rostomily, R.C., Alvord, E.C., 2008. A mathematical modelling tool for predicting survival of individual patients following resection of glioblastoma: a proof of principle. *Brit. J. Cancer* 98 (1), 113.
- Tanaka, M.L., Debinski, W., Puri, I.K., 2009. Hybrid mathematical model of glioma progression. *Cell Proliferat.* 42 (5), 637–646.
- Tosin, A., Preziosi, L., 2010. Multiphase modeling of tumor growth with matrix remodeling and fibrosis. *Math. Comput. Model.* 52 (7–8), 969–976.
- Tuch, D.S., Reese, T.G., Wiegell, M.R., Wedeen, V.J., 2003. Diffusion MRI of complex neural architecture. *Neuron* 40 (5), 885–895.
- Wang, C.H., Rockhill, J.K., Mrugala, M., Peacock, D.L., Lai, A., Jusenius, K., Wardlaw, J.M., Cloughesy, T., Spence, A.M., Rockne, R., Alvord, E.C., 2009. Prognostic significance of growth kinetics in newly diagnosed glioblastomas revealed by combining serial imaging with a novel biomathematical model. *Cancer Res.* 69 (23), 9133–9140.
- Wrensch, M., Minn, Y., Chew, T., Bondy, M., Berger, M.S., 2002. Epidemiology of primary brain tumors: current concepts and review of the literature. *Neuro-oncology* 4 (4), 278–299.
- Zinn, P.O., Majadan, B., Sathyam, P., Singh, S.K., Majumder, S., Jolesz, F.A., Colen, R.R., 2011. Radiogenomic mapping of edema/cellular invasion MRI-phenotypes in glioblastoma multiforme. *PloS One* 6 (10), e25451.